ADVANCED ENERGY MATERIALS
www.advenergymat.de

Kinetics and Pore Formation of the Sodium Metal Anode on NASICON-Type $Na_{3.4}Zr_2Si_{2.4}P_{0.6}O_{12}$ for Sodium Solid-State Batteries

*Till Ortmann, Simon Burkhardt, Janis Kevin Eckhardt, Till Fuchs, Ziming Ding, Joachim Sann, Marcus Rohnke, Qianli Ma, Frank Tietz, Dina Fattakhova-Rohlfing, Christian Kübel, Olivier Guillon, Christian Heiliger, and Jürgen Janek**

In recent years, many efforts have been made to introduce reversible alkali metal anodes using solid electrolytes in order to increase the energy density of next-generation batteries. In this respect, $Na_{3.4}Zr_2Si_{2.4}P_{0.6}O_{12}$ is a promising solid electrolyte for solid-state sodium batteries, due to its high ionic conductivity and apparent stability versus sodium metal. The formation of a kinetically stable interphase in contact with sodium metal is revealed by time-resolved impedance analysis, in situ X-ray photoelectron spectroscopy, and transmission electron microscopy. Based on pressure- and temperature-dependent impedance analyses, it is concluded that the $Na|Na_{3.4}Zr_2Si_{2.4}P_{0.6}O_{12}$ interface kinetics is dominated by current constriction rather than by charge transfer. Cross-sections of the interface after anodic dissolution at various mechanical loads visualize the formed pore structure due to the accumulation of vacancies near the interface. The temporal evolution of the pore morphology after anodic dissolution is monitored by time-resolved impedance analysis. Equilibration of the interface is observed even under extremely low external mechanical load, which is attributed to fast vacancy diffusion in sodium metal, while equilibration is faster and mainly caused by creep at increased external load. The presented information provides useful insights into a more profound evaluation of the sodium metal anode in solid-state batteries.

1. Introduction

In view of the worldwide increasing demand for storage and supply of electrical energy, the development of powerful rechargeable postlithium-ion energy storage concepts is intensifying.[1] Sodium-based battery concepts are gaining more attention in research due to the high abundance, feasible accessibility, and low reversible standard potential (E_H(Na) = −2.71 V vs standard hydrogen electrode) of sodium. In particular, to increase the energy density of current sodium-ion batteries huge efforts are made to replace hard carbon (roughly 530 mAh g^{-1})[2] with the sodium metal anode (1165 mAh g^{-1}).[3,4] However, side reactions and the formation of dendrites leading to capacity loss, short circuits, and cell failure have so far prevented the use of sodium metal anodes in room temperature liquid electrolyte-based batteries.[5]

Inorganic ceramic solid electrolytes (SE) like Na-β''-alumina (BASE) or

T. Ortmann, S. Burkhardt, T. Fuchs, J. Sann, M. Rohnke, J. Janek
Institute for Physical Chemistry
Justus Liebig University Giessen
35392 Giessen, Germany
E-mail: juergen.janek@phys.chemie.uni-giessen.de

T. Ortmann, S. Burkhardt, J. K. Eckhardt, T. Fuchs, J. Sann, M. Rohnke, C. Heiliger, J. Janek
Center for Materials Research (ZfM)
Justus Liebig University Giessen
35392 Giessen, Germany

The ORCID identification number(s) for the author(s) of this article can be found under https://doi.org/10.1002/aenm.202202712.

DOI: 10.1002/aenm.202202712

J. K. Eckhardt, C. Heiliger
Institute for Theoretical Physics
Justus Liebig University Giessen
35392 Giessen, Germany

Z. Ding, C. Kübel
Technische Universität Darmstadt
64289 Darmstadt, Germany

Z. Ding, C. Kübel
Institut of Nanotechnology (INT) and Helmholtz Institut Ulm (HIU)
Karlsruhe Institute of Technology (KIT)
76344 Eggenstein-Leopoldshafen, Germany

Q. Ma, F. Tietz, D. Fattakhova-Rohlfing, O. Guillon
Forschungszentrum Jülich GmbH
Institute of Energy and Climate Research
Materials Synthesis and Processing (IEK-1)
52425 Jülich, Germany

D. Fattakhova-Rohlfing
Department of Engineering and Center for Nano integration
Duisburg-Essen (CENIDE)
Universität Duisburg-Essen
47057 Duisburg, Germany

$Na_3Zr_2Si_2PO_{12}$ (NZSPO) are often discussed as a possible solution to overcome this issue since their high mechanical strength may prevent the growth of dendrites through the separator.[6] Additionally, replacing potentially toxic and flammable liquid electrolytes by inorganic solid electrolytes may enhance safety and environmental compatibility.[7]

NZSPO belongs to a solid solution with the general composition $Na_{1+x}Zr_2Si_xP_{3-x}O_{12}$ ($0 < x < 3$) and was first synthesized in 1976.[8,9] Compared to BASE with its highly anisotropic layered structure, advantages of NZSPO are its 3D conduction pathways and lower sintering temperature for achieving a comparable ionic conductivity of 0.7 mS cm^{-1} at 25 °C.[9] In recent years, lots of efforts have been made to improve the ionic conductivity of NZSPO up to 4 mS cm^{-1} (25 °C) through a wide variety of doping and synthesis protocols.[10–13] An optimum ionic conductivity is obtained at a Na^+ content of $x \approx 3.3$ per formula unit, which can be explained by an enhanced correlated migration process.[14] This compositional optimization was already reported in 1979,[15] but did not find attention in the scientific community. However, it recently motivated the re-investigation of the above solid solution and resulted in the ionic conductivity of 5.5 mS cm^{-1} (25 °C) for the composition $Na_{3.4}Zr_2Si_{2.4}P_{0.6}O_{12}$ (NZSP0.4).[16]

Unfortunately, contact of sodium metal with SEs often results in a large interfacial resistance R_{Int}, due to impeded ion transport across the interface, which degrades the cell performance. To reduce R_{Int} various approaches such as the introduction of artificial interlayers and coatings or surface treatments have been applied. In the case of BASE and NZSPO, the interfacial resistance R_{Int} was reduced from a few kΩ cm^2 to a several tens or hundreds Ω cm^2 using various interlayers based on polymers,[17,18] titanium dioxide,[19] graphene,[20] cotton fibers,[21] AlF_3,[22] or tin coatings.[23,24] A similar reduction of R_{Int} is achieved by improving the interfacial contact due to high external stack pressures or a reduced surface tension of Na by employing Na/SiO_2 composite anodes.[25,26] Removing surface contaminations like carbonates and hydroxyl groups by heat treatments decreases the interfacial resistance R_{Int} < 15 Ω cm^2.[27,28] In recent reports, Ma et al. reduced the interfacial resistance of NZSP0.4 below 1.0 Ω cm^2, which is attributed to a self-forming thin Na_3PO_4 layer formed on the surface of the ceramic during sintering.[16,29,30] However, a detailed analysis and interpretation of the Na|NZSP0.4 interface is still missing.

The term "interfacial resistance" R_{Int} is often used in the literature as a general term assigned to an impedance contribution in the medium- and low-frequency range of the spectrum, describing the interfacial behavior of a metal|SE interface. Unfortunately, mostly it is not properly considered that the "interfacial resistance" is composed of different processes including charge transfer (CT) processes, formation of a solid electrolyte interphase (SEI) and current constriction (CC). Especially, the CC phenomenon is not well established in the field of all-solid-state batteries and therefore often neglected. For the Na|BASE and Li|$Li_{6.25}Al_{0.25}La_3Zr_2O_{12}$ (LLZO) interface, it has been shown that an increase in resistance/overvoltage occurs primarily due to pore formation near the interface.[31,32] As insufficient contact at the "parent" metal|SE interface leads to the CC phenomenon, it is likely that the measured interfacial contribution estimated by impedance spectroscopy is dominated by CC.[28,33]

In contrast to the charge transfer process or the ion transport within the SE, the CC effect is not an independent microscopic electric migration process, but rather a mere geometric effect. CC occurs at spatially distributed microcontacts between the metal anode and the solid electrolyte separator, where dissolution and deposition of the metal take place. It strongly depends on the interfacial morphology as recently systematically studied by Eckhardt et al.[34,35] According to their work, CC should be distinguished in "dynamic" and "static" constriction: The impact of dynamic constriction depends on the excitation frequency of an applied electric AC field, while the static constriction effect is independent of external influences, e.g., when the electrode area is smaller than that of the SE.[34,35] Especially dynamic CC is strongly affected by the interfacial morphology of pores formed during anodic dissolution. The presence of microcontacts, however, does not require anodic dissolution to occur, since it can also originate from insufficient physical contact upon cell assembly or incomplete insulating interlayers like surface contaminations.[36,37] Evidence for CC can arise from a similar activation energy for the apparent interface resistance and the ion transport within the SE, as this indicates transport limitation by the SE in the constriction zone.[38] For the Na|NZSPO interface, significantly different activation energies $E_{a,Int}$ have been reported (0.6 eV[26] and 0.39 eV[39]) which were not assessed with respect to the corresponding bulk properties. Activation energies can vary significantly depending on the manufacturing process of the SE (microstructure) as well as on electrode preparation.[40]

With respect to the formation of microcontacts at the metal|SE interface under an external current load, it is worth noting that kinetic studies of the anodic dissolution of metals at a solid|solid phase boundary have been part of research decades ago. For instance, processes taking place during the anodic dissolution of the "parent" metals (Me) Ag and Cu at the Me|SE phase boundary and the resulting changes at the interface have been investigated in detail.[41–43] Anodic dissolution of metals at the phase boundary leads to the formation of metal vacancies at the interface between both solids. Without an external load the regeneration of the original interface can be achieved by the diffusion of vacancies into the bulk or diffusion-based creep mechanisms like Coble and Nabarro–Hering creep.[41,44] In case of faster dissolution compared to the regeneration of the interface, the contact area will be reduced and no stationary state is reached. Despite the decrease of the contact area, metal dissolution can occur by anodic dissolution of ad-atoms, which are transported to the interface by surface diffusion along the pore walls. By dissolving these metal atoms, extended pores are formed, which in turn affect the current distribution at the interface.[42] Additionally, surface diffusion allows size equilibration of formed pores driven by the minimization of the surface energy, which is similar to the Ostwald ripening of particles ("electrochemical Ostwald ripening").[45]

The mechanical stability of the interface is affected by the pores formed during anodic dissolution. Movement and relaxation of dislocations in the metal may breakdown the pore morphology even causing oscillatory effects at the interface.[41] These effects

C. Kübel
Karlsruhe Nano Micro Facility (KNMF)
Karlsruhe Institute of Technology (KIT)
76344 Eggenstein-Leopoldshafen, Germany
O. Guillon
Jülich Aachen Research Alliance
JARA-Energy
52425 Jülich, Germany

are even more pronounced when external load is applied since higher strain rates are achieved by different creep mechanisms.[44] Especially for sodium, creep is enhanced due to low yield strength and high homologous temperature (T_h = 0.8) at ambient temperatures.[46,47] Additionally, the grain size and dislocation density affect the mechanical properties such as yield strength and therefore influences the interfacial kinetic behavior.[48]

Superposition of different phenomena like interfacial degradation, charge transfer, current constriction, as well as regeneration under current load may take place simultaneously at the Na|NZSP0.4 interface. However, a systematic study to distinguish these processes is still missing in literature. It is worth to add that the formation of a highly heterogeneous interface during anodic dissolution (discharge of the cell) will cause highly inhomogeneous current distributions during subsequent cathodic deposition (plating, during charge of the cell), and therefore, will inevitably cause cell failure.

To answer the open questions and get deeper insight into the sodium anode kinetics on NZSP0.4, we performed a series of experiments under various conditions. First, we consider the thermodynamic stability of NZSP0.4 against sodium metal and analyzed the interface using time-resolved impedance analysis combined with in situ X-ray photoelectron spectroscopy (XPS) and transmission electron microscopy (TEM).

Second, we studied the kinetics of the anodic sodium dissolution by pressure- and temperature-dependent impedance analysis. Clearly, the interface contribution observed by impedance spectroscopy is mainly caused by insufficient mechanical contact.[34,35] Based on these results, CC is identified as dominated process at the interface rather than SEI formation and CT process.

Third, anodic dissolution is examined electrochemically under different external (mechanical) loads, and the interface is visualized on the basis of cross sections using focused ion beam scanning electron microscopy (FIB-SEM) and prepared under cryogenic conditions. In vacuum with low external loads ($p = 10^{-3}$ Pa), lens-shaped pores were observed, whereas at higher loads (p = 0.3 MPa), no regular structures can be identified. Finally, the temporal development of the dissolved interface is analyzed electrochemically and equilibration of the interface is observed at open-circuit voltage (OCV).

2. Results and Discussion

2.1. Stability of $Na_{3.4}Zr_2Si_{2.4}P_{0.6}O_{12}$ Versus Na

From a theoretical point of view, the electrochemical stability window of $Na_{1+x}Zr_2Si_xP_{3-x}O_{12}$ with x = 2 extends from ≈1 to 3.4 V versus Na^+/Na.[49,50] Increasing the Si/P ratio decreases the thermodynamic driving force of the decomposition in contact with sodium.[51] A similar shift for the stability window is obtained by density functional theory calculation.[52] To date, only $Na_3Zr_2Si_2PO_{12}$ has been investigated experimentally for its stability. Although apparently the same compound was used in various studies, the resistances obtained for the formed interphase range from tens of Ω cm² to several hundred Ω cm².[39,52,53] Likewise, the temporal development of the interphases differs significantly in the studies, too. Due to these variations, NZSP0.4 in contact with sodium is analyzed in detail. A detailed characterization of the used solid electrolyte material is given in Figure S1 (Supporting Information).

2.1.1. Time-Dependent Impedance Analysis of the Na|NZSP0.4 Interface

For time-dependent impedance analyses, symmetrical Na|NZSP0.4|Na cells were assembled in a specially designed pressure setup (see the Experimental Section for a more detailed description). Experiments were conducted in an Ar-filled glovebox to ensure immediate impedance recording after assembly (time delay <1 min). In **Figure 1**a, the development of the total impedance over time is depicted. After assembly one semicircle with an apex frequency of 1.57 MHz and a corresponding capacity of 4.5 nF cm^{-2} can be identified in the Nyquist plot. The observed contribution is attributed to grain boundary transport (GB) within the solid electrolyte, as the bulk transport process is beyond the measured frequency range (see Figure S2, Supporting Information). During data acquisition, only slight changes in the apex frequency (1.4 MHz) and the capacitance (4.3 nF cm^{-2}) were observed, while the real part of the impedance increases by 6 Ω cm². No additional and clearly

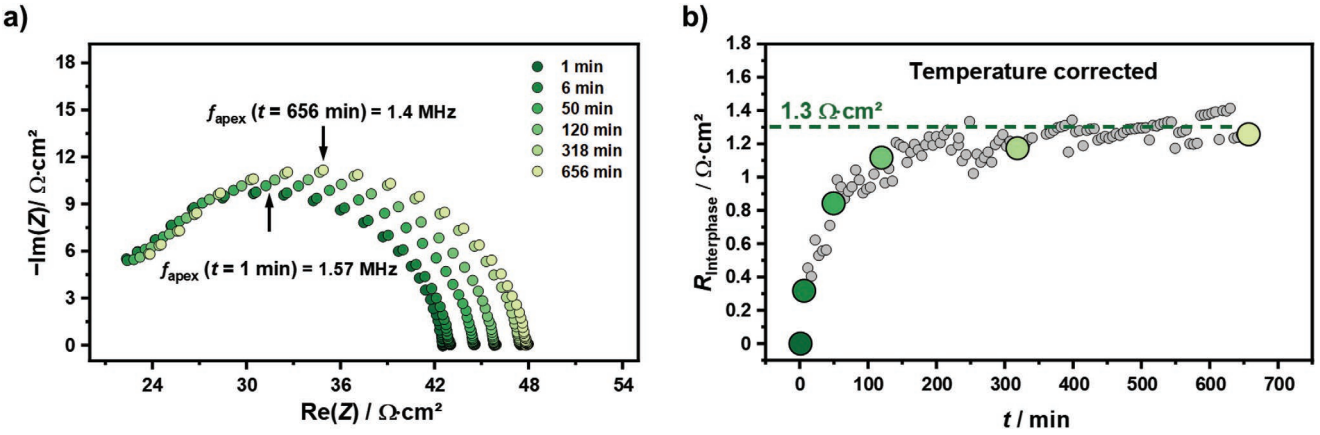

Figure 1. a) Time evolution of the impedance of a symmetrical Na|NZSP0.4|Na cell. Time delay between assembly and recording was <1 min. b) Temporal development of the temperature-corrected resistance of the interface (gray) and the corresponding values determined from the impedance spectra depicted in a) (green). Elimination of temperature fluctuations relies on the temperature dependence of the bulk and grain boundary impedance of the SE. A detailed description can be found in the Supporting Information.

separated contribution in the impedance data—which could indicate the formation of an interphase—was observed. However, it might be possible that the time constants of the GB and the interphase impedance are too close or that the impact of the interphase is below the detection limit given by the experimental setup used.

We like to note (see the Experimental Section) that the impedance measurements were conducted in a glovebox, as transfer to a climate chamber would have taken too long. While this helped to quickly observe the impedance after cell assembly, the glovebox was not perfectly temperature-controlled. A temperature-correction for the measured impedance data was carried out to verify that the observed resistance increase is not caused by the temperature-dependence of the ionic conductivity of NZSP0.4. A detailed description of the procedure is given in Figure S3 (Supporting Information).

The temperature-corrected impedance spectra measured under equilibrium conditions show that any interphase resistance $R_{\text{Interphase}}$ is negligibly small as can be seen in Figure 1b. Additionally, the time dependence of $R_{\text{Interphase}}$ indicates a self-limiting behavior. When the measurement was repeated three times, a mean resistance increase of about 1.3 Ω cm^2 was observed due to interphase growth (for details see Figure S3b,c, Supporting Information).

However, as a high uncertainty is obtained for $R_{\text{Interphase}}$ from a formal error analysis, the same experiments were also carried out in a controlled temperature environment. Sealing and temperature stabilization of the cell to 25 °C led to a time delay of 18 min between assembly and start of data acquisition. A similar increase of the total impedance as well as a similar time course support the previous results, as shown in Figure S3d (Supporting Information). We assume that this small change in resistance is indeed caused by degradation at the Na|NZSP0.4 interface, i.e., by SEI formation.

2.1.2. In Situ XPS and TEM Characterization of the Na|NZSP0.4 Interface

To investigate the degradation processes at the Na|NZSP0.4 interface, chemical and structural analyses were carried out by in situ XPS and TEM. First, the surface of the pristine NZSP0.4 was characterized by XPS. Detail spectra of the elements in the SE as well as the C 1s signal are depicted in Figure S4 (Supporting Information). The binding energies (BE) obtained are in good agreement with those of NZSPO.[26,52,53] Since the substitution of $(PO_4)^{3-}$ by tetrahedral $(SiO_4)^{4-}$ in the crystal structure does not affect the chemical environment of phosphorous and silicon, no shifts in binding energy were expected and this is confirmed by the experimental data. When NZSPO is exposed to ambient atmosphere a contamination layer containing carbonates and hydroxyl groups is formed.[27,54] Along the C 1s spectrum, mainly C–C bonds and a small fraction of C–O bonds were found, probably originating from the residual atmosphere inside the XPS chamber. As no further signal (e.g., carbonate) is identified in the C 1s spectra, the presence of a surface contamination layer is excluded for the material investigated.

Chemical changes of the interface by successive deposition of sodium on NZSP0.4 via sputter deposition inside the XPS chamber were monitored by intermittent XPS. **Figure 2**a–c depicts the development of the Zr 3d, Na 1s, and O 1s signals with increasing amount of deposited sodium. The evolution of a shoulder at lower binding energies in the Zr 3d signal indicates the reduction of Zr^{4+} to Zr suboxides by deposited sodium (Figure 2a). Figure 2d shows the corresponding fit of the last XP spectrum, where the shoulder at lower binding energies is described using two suboxides compounds with binding energies of E_b(Zr 3d) = 180.9 eV and E_b(Zr 3d) = 180.0 eV. Similar binding energies have been reported for the Zr signal in the case of $Na_3Zr_2Si_2PO_{12}$ after contacting with sodium metal.[39,52] Accordingly, the signal at E_b(Zr 3d) = 180.0 eV would indicate a species with an oxidation state between Zr^{1+} and Zr^{2+}, whereas the signal at E_b(Zr 3d) = 180.9 eV indicates species with an oxidation state between Zr^{2+} and Zr^{3+}.[55,56] A reliable identification of reduced Zr species is challenging as more suboxides could be present or phases with varying oxygen content formed leading to broadening of the signal. However, to analyze the development of the reduced Zr species during sodium deposition, we assume to have only two suboxides.

As shown in Figure 2e, after 15 min of sodium deposition, no change in the relative atomic fractions of Zr 3d(SE) and Zr 3d(sub-oxides) was observed. Based on the signal attenuation of the Zr 3d region, roughly 1 nm of Na had been deposited after 15 min, indicating a very thin interfacial layer.

XP spectra of the Si 2p and P 2p regions are shown in Figure S5 (Supporting Information). Only in the first Si 2p spectrum a slightly asymmetric peak shape was observed, which is probably caused by a cleaning step of the surface using an argon sputter gun. Due to the similar binding energy (E_b(Si 2p) = 101.0 eV) compared to an untreated surface (E_b(Si 2p) = 101.2 eV, see Figure S4c, Supporting Information) the effect can be neglected. However, apart from attenuation, no changes in the XP spectra were detected in the Si 2p region during sodium deposition, as well as in the P 2p region. Consequently, Si and P are either not reduced or they form volatile and unstable decomposition products that cannot be detected by XPS.[52]

Before deposition, only one signal at E_b(Na 1s) = 1071.1 eV was observed in the Na 1s region, which is assigned to sodium ions (Na^+ signal) in the SE (Figure 2b). After the first deposition cycles, a shoulder appears at lower BE of the Na 1s line, which develops into a separated line with a binding energy E_b(Na 1s) = 1069.1 eV. This is evidence for the formation of metallic sodium on the SE, which can be confirmed by the observation of plasmon patterns at binding energies of E_b(Na 1s) = 1074.9 eV and E_b(Na 1s) = 1080.8 eV.[57] The area below the sodium signal increases after the first deposition of sodium metal. Since differences in BE between different Na^+ ion-containing compounds are very small (<0.5 eV), a differentiation is challenging. However, an oxidation of freshly deposited sodium can be inferred from the increase in area.

The evaluation of the O 1s signal, shown in Figure 2c, is complicated due to superposition with sodium Auger electrons. In addition, depending on the chemical environment, sodium Auger electrons have different energies.[58] Therefore, refer-

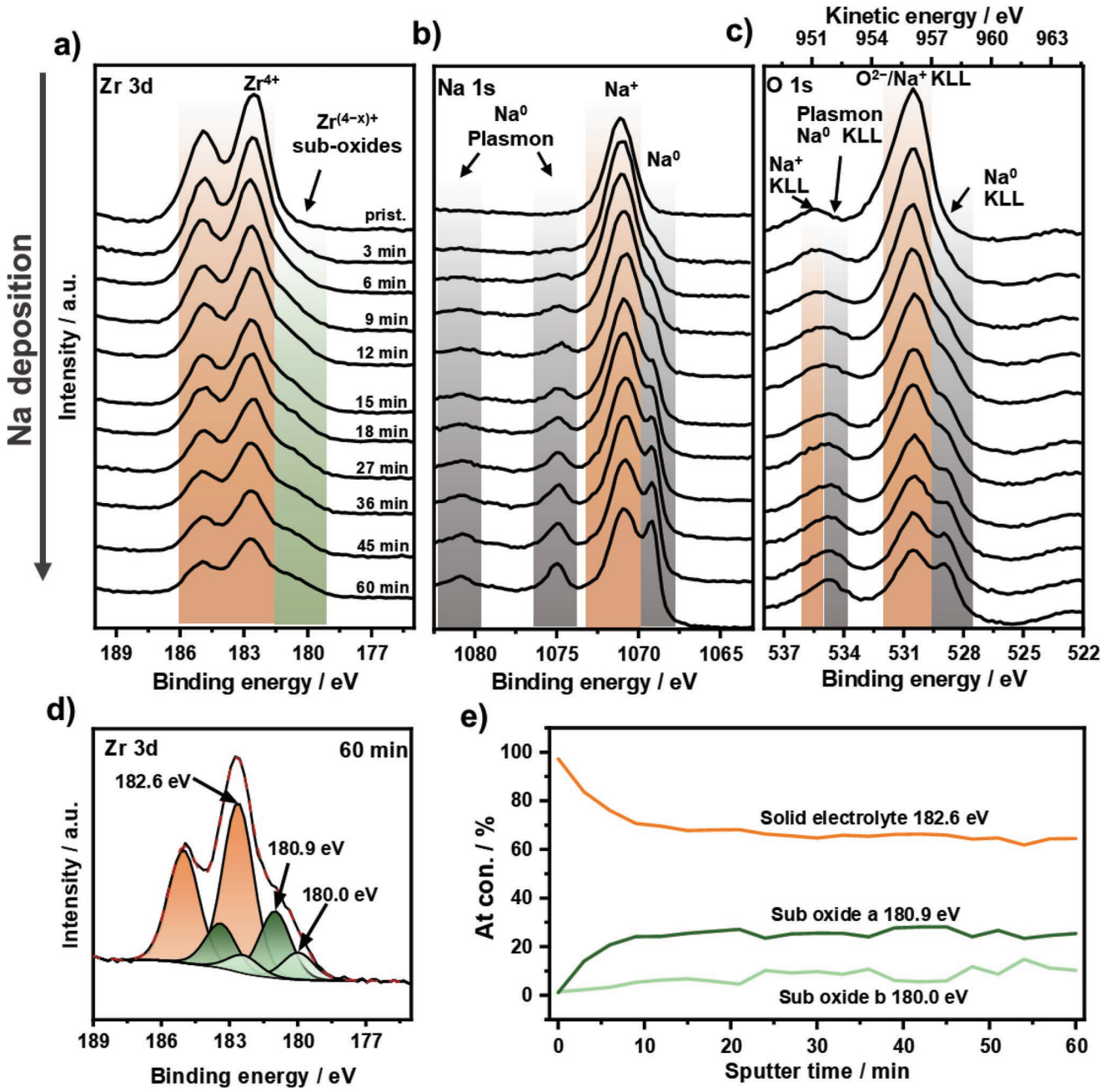

Figure 2. a–c) XP spectra of Zr 3d, Na 1s, and O 1s after different sodium deposition times. Binding energies of the SE, metallic sodium, and reduced spices are highlighted in orange, gray, and green, respectively. The color coding is maintained in d) and e). d) Detail spectra of Zr 3d after a sodium deposition time of 60 min. Beside the main peak of the SE two further suboxide signals at 180.9 and 180.0 eV are used for fitting of Zr 3d signal. e) Relative atomic concentrations in the Zr 3d region with increasing deposition time of sodium. After 15 min, no further change in the composition of the Zr 3d signal was detected indicating a self-limiting reaction.

ences of sodium Auger emissions are necessary to assess their influence in the O 1s region and to interpret the O 1s spectrum properly. Assuming that Auger electrons of Na^+ have a similar kinetic energy, Na_2O can be used as a reference material to distinguish between Na^0- and Na^+-KLL emissions. Hence, the signal at E_b = 535.6 eV (E_{Kin}(photoelectron(PE)) = 951.0 eV) can be ascribed to the Auger process Na^+-$KL_1L_{2,3}$.[59] The main signal at E_b = 530.5 eV originates from the oxygen lattice of the SE and attenuates with increasing deposition time. This signal includes Na^+ Auger electrons, which is obvious from the emission pattern, making reliable fitting challenging.[59] Therefore, the formation of Na_2O postulated by Gao et al. cannot be confirmed based on the results obtained.[54] Finally, the formation of metallic sodium was observed by the Na^0-$KL_1L_{2,3}$ emission at E_{Kin}(PE) = 957.6 eV with an associated plasmon at E_{Kin}(PE) = 951.9 eV.

By comparing the sodium signals (PE and Auger electrons) obtained from metallic sodium with a reference sample (freshly prepared sodium foil) calibrated to the Fermi level, a shift of roughly 2.5 eV to lower energies was found as can be seen in Figure S6 (green curves) as well as Tables S1 and S2 (Supporting Information). For Na|NZSPO interface a band bending of 0.1–0.6 eV due to the formation of a degradation layer at the interface has already been reported.[54,60] However, a band bending of 2.5 eV in the case of NZSP0.4 is rather unlikely, which is why we suspect an additional effect. When sodium is placed on an electronically insulating tape a similar shift of about 2.3 eV for the metallic sodium signals, including the Fermi level, to lower BE is observed (Figure S6 light orange curves, Supporting Information). Therefore, we suspect that the observed shift is mainly a sodium-specific effect in combination with electronically insulating measurement setups. We assume that an equilibration of Fermi levels of sodium in contact with electronically insulating material does not occur. The shift of 2.2–2.3 eV is close to the open circuit voltage of a sodium-oxygen cell (2.27–2.33 V).[61] As residual oxygen is present inside the XPS chamber, the formation of Na_2O in contact with sodium is likely. As Na_2O is a poorly conducting solid electrolyte and if thin enough, it can separate sodium metal from residual oxygen, thus forming a sodium-oxygen cell. During XPS measurements the surface potential is set to zero by the applied neutralization. Referencing to the cathode active material (which might be Na_2O_2, NaO_2, or O_2) leads to a lowering of the Fermi level in the sodium electrode, resulting in a lower binding energy. Despite a very low oxygen partial pressure inside the XPS chamber, a potential difference of roughly 1.95–2 V can be expected for a local sodium-oxygen galvanic cell.[62] A superposition of both effects might be a possible explanation for the observed shift.

The newly formed Na|NZSP0.4 interface was characterized 8 h after the last step of sodium deposition. As shown in Figure S7 (Supporting Information), no further changes in the Zr 3d, Si 2p, and P 2p signals were observed. Only a decrease of the metallic sodium signals in the Na 1s and O 1s region is found, which is due to the reaction with residual atmosphere (especially oxygen). This is shown by quantifying the absolute signal areas in Table S3 (Supporting Information), since the amount of oxygen increases while all other areas remain unchanged.

To analyze and visualize the morphology and thickness of the interfacial degradation layer, TEM characterization was conducted. For the sample preparation a symmetric Na|NZSP0.4|Na cell was assembled and stored until the formation of the interphase has been finished. To excavate the interface by removing one electrode without damaging the formed interphase, one sodium electrode was anodically dissolved. Immediately after removal, a copper layer (120 nm) was deposited thermally on the exposed interface as protection layer to avoid changes. In addition, a Pt layer was deposited for the preparation of the electron transparent lamella by FIB milling technique. A detailed description of the preparation is given in Section S5 and Figure S8, Supporting Information).

The lamella was tilted until the surface of the NZSP0.4 was aligned parallel to the electron beam and high-angle annular dark-field (HAADF) scanning transmission electron microscopy (STEM) images were recorded. Besides the NZSP0.4 (**Figure 3**a, right side) and the deposited protection layer (Figure 3a, left side), an additional layer on the surface of the SE with an increased signal intensity can be observed in the HAADF image. However, clear identification of the formed interphase is not possible as no clear morphology change compared to the SE is found. Therefore, energy-dispersive X-ray spectroscopy (EDX) analysis was performed to characterize the elemental distribution of the layered system. The measured region is highlighted in Figure 3b and the corresponding spectra are shown in Figure 3c.

A similar elemental composition is obtained for the protection layer (region A) as well as the bright layer on the surface of the NZSP0.4 (region B) which mainly consist of sodium, oxygen, copper and platinum. As no zirconium (Zr-K_α line, Zr-L_α overlap with Pt-M_α line) and only slight amounts of silicon are observed in region B, we do not suspect that this interphase originate from the degradation of NZSP0.4 in contact with sodium, since a formed interphase should contain all the elements of the participating reactants.

The presence of sodium and oxygen in the region A and B originates from the preparation process of the specimen as residual sodium will be left at the surface after removing the sodium electrode. Despite a copper protection layer, the residual sodium degrades even in inert atmosphere during further preparation of the lamella. Additionally, the preparation process also explains the presence of platinum directly on the surface of NZSP0.4 as the copper layer does not have a proper contact to the SE and deposition of platinum into the gap is likely to occur during preparation of the lamella.

Finally, the regions near the surface (C) and the bulk (D) of the NZSP0.4 sample were analyzed. Comparing both spectra, a similar elemental composition is observed indicating that no changes in the near-surface region of the SE occurred. A reliable quantification of the SE is not possible as the P signal cannot be clearly separated from the Zr-L_α signal. All other elements of the NZSP0.4 can be identified in the spectra. The presence of a Cu signal in regions C and D is probably due to the copper background of the cryo transfer holder. The experiment was repeated for a second specimen showing similar results as can be seen in Figure S9 (Supporting Information).

In summary, when contacting NZSP0.4 with sodium a kinetically stabilized interphase is formed, which appears to prevent further degradation of NZSP0.4. This interphase causes a minor increase of $R_{\text{Interphase}}$ by about 1.3 Ω cm^2 and could not be identified well via TEM. We therefore assume that NZSP0.4 forms a very thin kinetically stable interface with a low charge transfer resistance.

2.2. Charge Transfer and Current Constriction at the Na|NZSP0.4 Interface

Different processes take place at the interface influencing the interfacial kinetics such as charge transfer, space charge layer formation, defect relaxation, crystallization phenomena, diffusion, or current constriction.[38] Usually, any low-frequency impedance of the Na|NZSPO interface is considered as an interface-related impedance and assigned to charge transfer, however, without clear proof.[20,24,54] As discussed in the

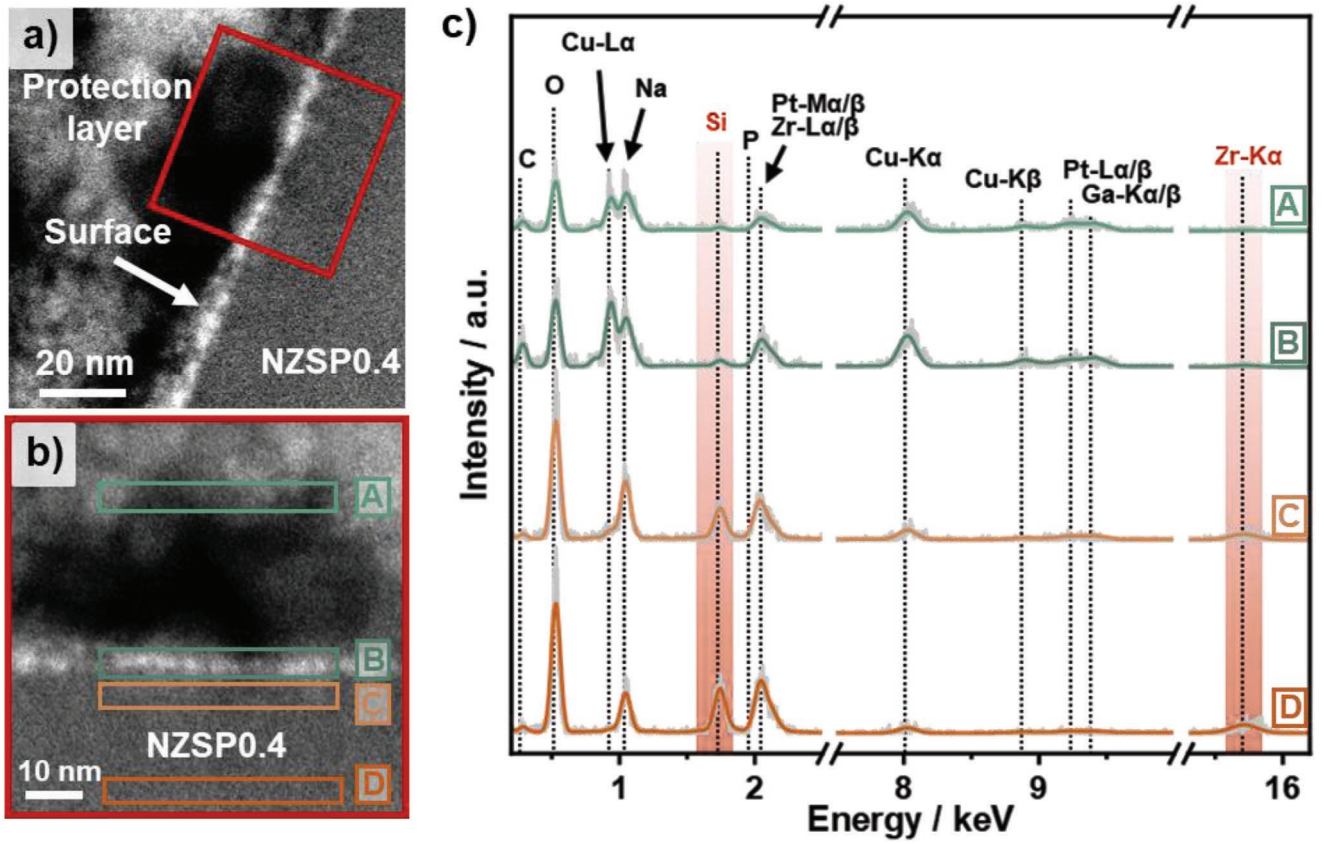

Figure 3. a) High-angle annular dark-field (HAADF) scanning transmission electron microscopy (STEM) image of the prepared electron transparent lamella from the Na|NZSP0.4 interface. Based on different morphologies, the NZSP0.4 solid electrolyte separates clearly from the deposited protection layer. b) HAADF-STEM image of the red marked region in a) at higher magnification. c) Energy-dispersive X-ray spectroscopy (EDX) spectra of selected regions which are highlighted in green and orange in (b). The measured spectra are shown in light gray, while the model spectra are presented in the respective color (orange and green). No changes in the elemental composition are observed in the near-surface region of the NZSP0.4 compared to the bulk.

Introduction, contact loss and the rise of current constriction at a few remaining contact points lead to an additional impedance contribution in the low-frequency region. Pressure- and temperature-dependent potentiostatic electrochemical impedance spectroscopy (PEIS) analysis allows to estimate whether the effect of current constriction or charge transfer is dominating the overall interfacial resistance, as has been shown for the Li|LLZO interface.[33]

2.2.1. Pressure-Dependent PEIS Analysis of Na|NZSP0.4 Interface

The physical contact area between parent metal and the SE can be adjusted by applying external force (pressure). Since the interfacial contact area between parent metal and SE is proportional to the number of microcontacts, R_{Int} should decrease upon increasing the contact area, density, and size of microcontacts. To investigate the role of these microcontacts, a Na_{bc}|NZSP0.4|Na_{id} cell was assembled whereby one electrode has a low load-bearing contact area denoted as Na_{bc} in the following. The other sodium electrode, called Na_{id} (ideally reversible), can be seen as a quasi-reference electrode (QRE), as described in detail in the Experimental Section.

The contact at the Na_{bc}|NZSP0.4 interface was adjusted by applying external load to the Na_{bc}|NZSP0.4|Na_{id} cell. The external force was gradually increased, and each force was applied for 30 s. After each step, the force was released so that the interfacial contact area does not change during the impedance analysis. The obtained impedance spectra are shown in **Figure 4**a. With an initial force of roughly 1 N, clearly two semicircles are observed at an apex frequency of 1.08 MHz and 88 kHz and with capacitances of 4 and 34 nF cm^{-2}, respectively. The contribution in the high-frequency range can be assigned to the GBs in NZSP0.4 and the one in the lower-frequency range to the interface (see Section S2 for details, Supporting Information).

The impedance data were fitted with the equivalent circuit shown in Figure 4a. The results for the interfacial resistance R_{Int} and capacitance C_{Int} at different loads are shown in Figure 4b. Starting from R_{Int} = 53 Ω cm^2, the interfacial resistance declines with increasing force and becomes 7 Ω cm^2 at an applied force of 215 N (details for normalization are given in Section S6, Supporting Information). The changes in resistance with increasing external load are significantly larger compared to the small resistance of the electrode interphase (as determined in Section 2.1.1), and thus, we can neglect the latter. The

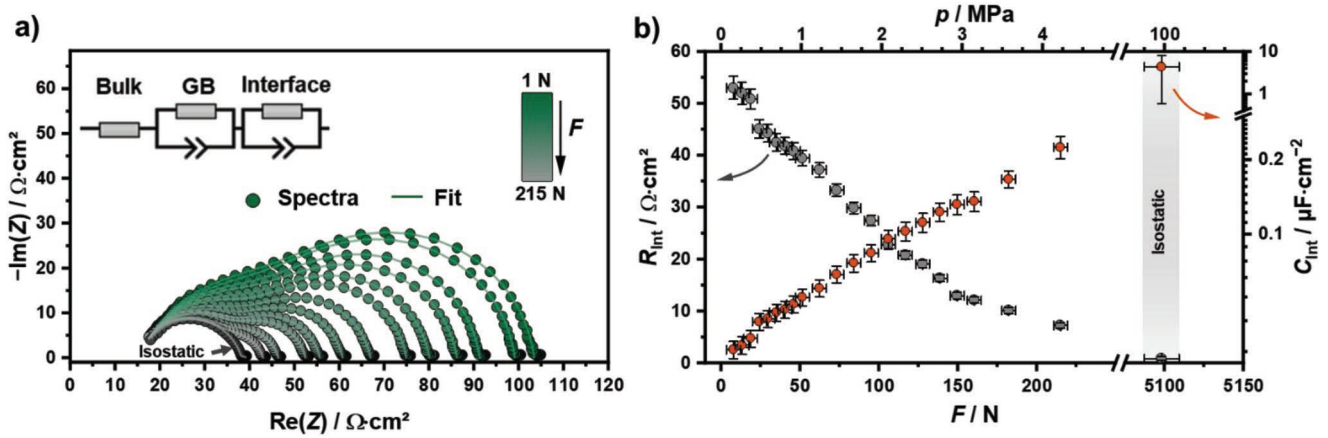

Figure 4. a) Impedance data of a sodium WE attached to a NZSP0.4|Na_{id} half-cell. The external force was gradually increased. At each step a uniaxial force was applied for 30 s. The impedance spectrum labeled with "isostatic" was obtained with an isostatic pressure of 100 MPa applied for 15 min. All impedance spectra were recorded at a base external force of 1 N to avoid changes of the contact area during the measurement. The equivalent circuit depicted in (a) was used for fitting of the impedance data, which is visualized as lines. b) Resistances and capacitances of the interface contribution as a function of the external force. Shown uncertainties originate from the fitting process and were given by the software used. With increasing force, the capacitance rises, whereas the resistance falls. The given pressure is estimated by the applied force and the geometric electrode area after the experiment.

local pressure on the scale of the microcontacts is unknown as the electrode and contact area of the sodium foil increases during force application due to plastic flow, and therefore, we prefer to report force rather than pressure. The pressure given in Figure 4b is related to the geometric electrode area after the experiment to give an estimate of the pressure.

At high isostatic pressures of 100 MPa, R_{Int} is significantly reduced to less than 1 Ω cm^2. However, an interfacial resistance can still be identified in the impedance spectrum, as can be seen from the asymmetric impedance shape in Figure 4a and is even more evident in the distribution of relaxation times (DRT) analysis (see Figure S10a and the Experimental Section for details, Supporting Information). The observed R_{Int} might be caused by degradation of the sodium electrode due to long exposure to glovebox atmosphere rather than to $R_{Interphase}$.

The interfacial capacitance shows an opposite trend compared to the resistance and rises with increasing force. This also indicates that the contact area between the sodium electrode and NZSP0.4 is increasing, i.e., the interfacial contact is improving, increasing the double layer capacitance at the interface.[34]

In addition to the external (mechanical) load during the contacting of sodium and SE, the time period and the directional anisotropy of the load (uniaxial vs isostatic) are also decisive for the interfacial contact. Three Na_{bc}|NZSP0.4|Na_{id} cells were assembled whereby different external loads at defined time periods were applied to prepare the working electrode (WE). The corresponding impedances are shown in **Figure 5**a.

Even at a uniaxial pressure of 1.7 MPa, no interfacial contribution was detected in the Nyquist plot, which is verified by DRT analysis (Figure S10b, Supporting Information). When the external load was increased to 11 MPa (uniaxial) or 100 MPa (isostatic), there was only a slight decrease in the total impedance of 2.5 Ω cm^2, which clearly shows that the interfacial contact is nearly optimal, even at low loads. A reason for this might be the surface roughness of the SE, as a rough surface leads to higher local stress and plastic flow even at minor external loads. When an ideal interfacial contact is already achieved at minor loads, further increase of pressure does not significantly reduce the total impedance.

The influence of the specific processing to establish the Na|NZSP0.4 interfacial contact gets even clearer when comparing a gradual load increase (Figure 4a) and a one-step load preparation protocol (Figure 5a). While a stepwise increase of the load yields an interfacial contribution of about 25 Ω cm^2 when reaching 1.7 MPa, no contribution was observed by a one-step load preparation. We interpret this apparent discrepancy as follows:

When sodium is pressed onto the SE, point contacts are initially present at the interface. Due to a significantly higher contact stress at these contact points compared to the bulk material, the dislocation density is locally increased. A higher dislocation density leads to strain hardening, which in turn requires higher pressures for the deformation of sodium. However, the locally increased dislocation density will decrease by recovery and recrystallization processes, which in turn proceeds with time. Therefore, strain hardening is normally not observed for sodium due to the high homologous temperature (T_h = 0.8) at ambient temperature, which enhances recovery. However, as high strain rates and short relaxation times (1 min) were used for the stepwise pressing, complete recovery is unlikely, resulting in strain hardening at the interface. Additionally, sodium gets harder by increasing the strain rate.[46] The recovery (annihilation of dislocations) and recrystallization is a function of time.[63] Second, the longer handling inside the glovebox of the previous experiment led to a formation of surface contaminations like sodium oxide. Such contamination may enhance the effective yield strength.[64] The formed contaminations may also explain the small but present interfacial contribution after applying a pressure of 100 MPa in the previous experiment compared to the impedance data shown in Figure 5a.

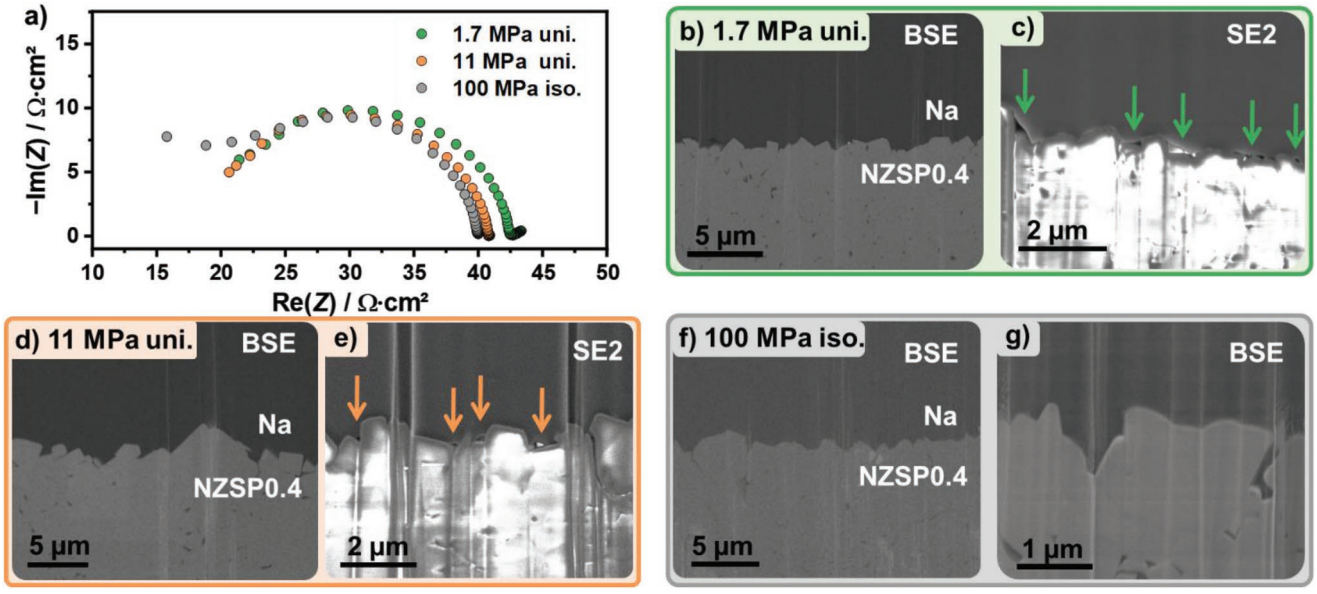

Figure 5. a) Impedance spectra of three different Na|NZSP0.4|Na_{id} cells with the WE pressed on the SE at 1.7 MPa for 60 s, 11 MPa for 60 s, and 100 MPa for 900 s. The abbreviations "iso." and "uni." represent isostatic and uniaxial pressure. For each pressure, cross-sections of the Na|NZSP0.4 interface are shown at low magnification b), d), and f) and at high magnification in (c), (e), and (g). Images described with BSE indicate a back-scattered electron image, whereas SE2 describes a secondary electron image. The arrows indicate pores at the Na|NZSP0.4 interface.

Cross-sections of Na|NZSP0.4 interfaces are shown in Figure 5b–g for differently applied pressures. For all pressures, full interfacial contact is seen in the backscattered electron images at low magnification level. However, by increasing the magnification, pores with a size of a few hundred nanometers are visible at the interface assembled with a pressure of 1.7 MPa. The number of pores as well as their size decreased after applying 11 MPa, but pores were still present. Only at an isostatic pressure of 100 MPa an apparently fully contacted interface was achieved without pores at the interface.

From a geometrical point of view, if an electrically insulating pore is present between the sodium and the SE, there should be a (dynamic) constriction-induced contribution in the resulting impedance spectra.[34,35] Surprisingly, despite the presence of pores at the interface at 1.7 and 11 MPa, the constriction contribution cannot be clearly identified in the associated impedances. One possible explanation for this could be the similar time constant of the pore-induced current constriction and that of the SE grain boundary transport process.

Current constriction is also affected by distribution of the contact area at the interface as a finer distribution leads to a less pronounced constriction effect in the impedances, i.e., the constriction resistance decreases.[34] A finer distribution minimizes the distance between the center of the contact spots and the centers of the pores. As can be seen in Figure 5c–e, pores are only formed in "valleys" due to the higher surface roughness of the SE (R_a = 0.19 µm). Thereto, smaller pores with a finer distribution are observed which may result in difficult separation of the CC signal and the GB transport contribution. Similar behavior has been observed at the Li|LLZO interface, where the CC signal vanishes almost completely despite a native passivation layer between metal electrode and the SE.[37] Accordingly, the surface roughness of the SE plays an important role for the impedance behavior of the metal|SE interface.

2.2.2. Temperature-Dependence of the Impedance

To gain a deeper understanding of the interfacial kinetics between sodium and NZSP0.4, temperature-dependent impedance analyses were performed. Three types of cells with different interfacial contact were analyzed and the activation energies E_a for each transport process including bulk, GB, and interface were determined based on the brick layer model.[65] The respective impedance spectra and Arrhenius plots are shown and discussed in Figure S11 (Supporting Information). The values for the activation energies determined are summarized in Table S4 (Supporting Information). Independent of the cell type (electrode material and interfacial contact) similar values of $E_{a,bulk}$ = 0.26 eV and $E_{a,GB}$ = 0.36 eV are obtained. Only for Na_{bc}|NZSP0.4|Na_{id} cells an additional interfacial contribution is observed in the low-frequency range with an activation energy $E_{a,Int}$ = 0.37 eV, which is quite similar to $E_{a,GB}$.

As mentioned above, non-ideal electrode contacts give rise to a constriction impedance, as recently discussed by Eckhardt et al.[34,35] In the following, we will discuss whether the concept of current constriction applies to the Na_{bc}|NZSP0.4 interface.

Pressure-dependent experiments demonstrate that poor interfacial contact is the major issue for a high interface-related resistance, which vanishes completely after increasing the external load. Additionally, no further contributions can be resolved by impedance analysis at near-ideal contact situations, and the bulk and GB activation barriers are similar to those of symmetrical Au|NZSP0.4|Au cells. This implies that the charge transfer between electrode, interlayer and solid electrolyte is not the rate-determining step. As shown in Section 2.1.1, any charge transfer step, even involving the thin SEI interlayer, corresponds to a resistance contribution of only about 1.3 Ω cm².

Due to current constriction, an inhomogeneous potential distribution is caused near the interface in the SE which

homogenizes when going into the bulk of the SE. Hence, the volume of the SE near the interface is influenced by the inhomogeneous potential, i.e., by current constriction.[34] The microstructure (grains and grain boundaries) within this volume strongly affects the activation energy of the constriction resistance, as the CC effect does not reflect an independent microscopic electric migration process. For the limiting case of a Na|single crystal SE interface a similar activation energy of bulk $E_{a,bulk}$ and constriction $E_{a,CC}$ is expected since the ion transport in the SE is the limiting step.[66,67] In the case of a Na|polycrystalline SE, grain boundaries affect the total conductivity. Depending on the grain boundary arrangement (number of grain boundaries at the interface and grain size) near the Na|SE interface and on the relaxation time of different charge transport processes, the activation energy of the constriction resistance $E_{a,CC}$ may approach that of the grain boundaries $E_{a,GB}$.[35,68] Therefore an activation energy between $E_{a,bulk}$ and $E_{a,GB}$ is expected for $E_{a,CC}$. Such a behavior has been observed for the Na|BASE interface as well as for the Li|LLZO interface.[28,33] In the case of the Na_{bc}|NZSP0.4 interface, $E_{a,Int}$ (0.37 eV) is equal to $E_{a,GB}$ and significantly larger than $E_{a,bulk}$ (0.26 eV). The higher activation energy of the interface $E_{a,Int}$ can be explained by two effects. Given the small grain size (see Figure S1, Supporting Information), the high GB density should result in an $E_{a,CC}$ close to $E_{a,GB}$.[35] Second, LLZO as well as BASE are stable in contact with their alkali metal, while this is not the case for NZSP0.4. Hence, the formed interphase will also influence the overall ion transport across the interface. Depending on the activation energy of the Na^+ ion transport through the formed interphase, $E_{a,Interphase}$, the determined $E_{a,Int}$ will be higher ($E_{a,Interphase} > E_{a,CC}$) or lower ($E_{a,Interphase} < E_{a,CC}$). If $E_{a,Interphase} > E_{a,CC}$, this would lead to a higher $E_{a,Int}$ even when the total increase in resistance is comparably small.

Based on these results, we conclude that charge transfer at the Na|NZSP0.4 interface is not the rate-determining step, but current constriction. The vanishing interface impedance at increased external loads as well as the similar values of $E_{a,Int}$ and $E_{a,GB}$ give evidence for this interpretation.

2.3. Na|NZSP0.4 Interface During Anodic Dissolution

Recent studies have shown that the overpotential at alkali metal|SE interfaces increases during anodic dissolution of the metal, while it remains unchanged during deposition.[31,69] The rising overpotential is explained by local loss of contact and the formation of pores at the interface. Hence, the pore formation during anodic dissolution is the limiting phenomenon during the cycling of metal|SE interfaces as inverting the current direction leads to dendrite formation due to current focusing. To monitor the evolution of the Na|NZSP0.4 interface during anodic dissolution, an alternating approach comprising chronopotentiometry (CP) and PEIS has been used as a dissolution protocol. During dissolution, the current density was incrementally increased from 67 to 340 μA cm^{-2}.

With proceeding dissolution, an additional contribution in the mid-/low-frequency range (<100 kHz) of the measured impedance spectra was observed in the Nyquist plots depicted in **Figure 6**a. This additional impedance contribution is attributed to the CC effect at the interface. The equivalent circuit depicted in Figure 6a was used for fitting the impedance data. The series resistance describing bulk transport in the solid electrolyte was assumed to be constant. The results are summarized in Figure 6b. Within the first 200 min, all resistances remain unchanged (see Figure 6b), which is in accordance with the constant potential curve depicted in Figure 6c. After 350 min, R_{Int} rises strongly until the experiment was finished, while R_{bulk} and R_{GB} do not change significantly. Clearly, R_{Int} is mainly responsible for the increasing overpotential (see Figure 6c) during anodic dissolution. C_{Int} decreases with increasing dissolution time highlighting the contact loss at the interface and is consistent with the described CC effect.[34,35] After reaching

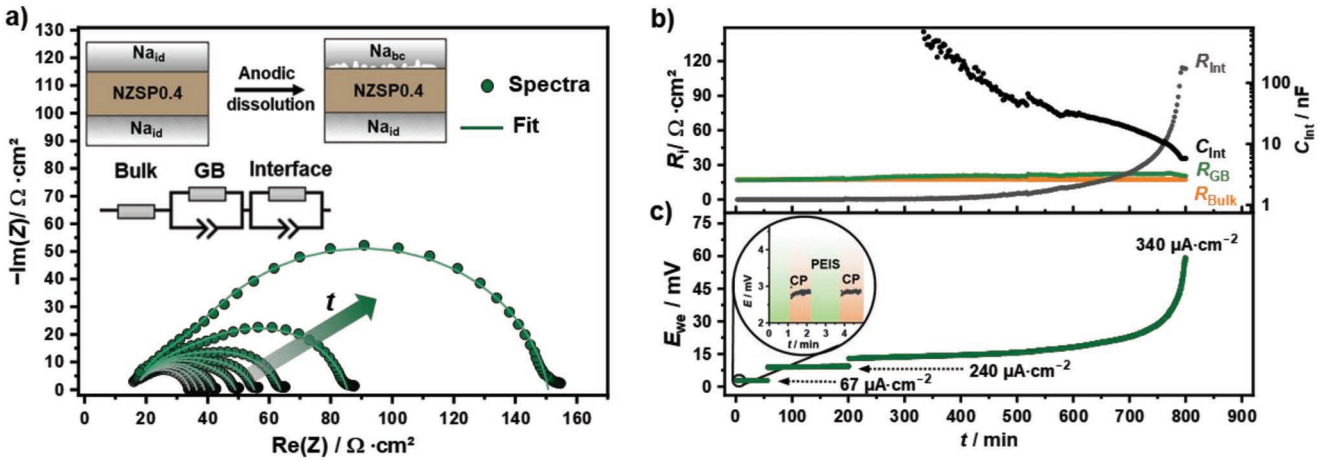

Figure 6. Anodic dissolution of sodium at the Na|NZSP0.4 interface with an applied uniaxial pressure of 11 MPa to gain an ideally reversible electrode (Na_{id}). The dissolution was conducted at 25 °C without external load, despite a small pressure required for contacting the current collectors. The sodium electrode was dissolved in intervals of 60 s by chronopotentiometry (CP) and then characterized by PEIS. a) Selected impedance spectra during anodic dissolution. With increasing dissolution time, an interface-related contribution forms at low frequencies. b) Temporal evolution of determined resistances for bulk, grain boundary, and interface as well as the capacitance of the interface. c) Voltage profile of the anodic dissolution at current densities of 67, 240, and 340 μA cm^{-2} up to a cut-off voltage of 60 mV.

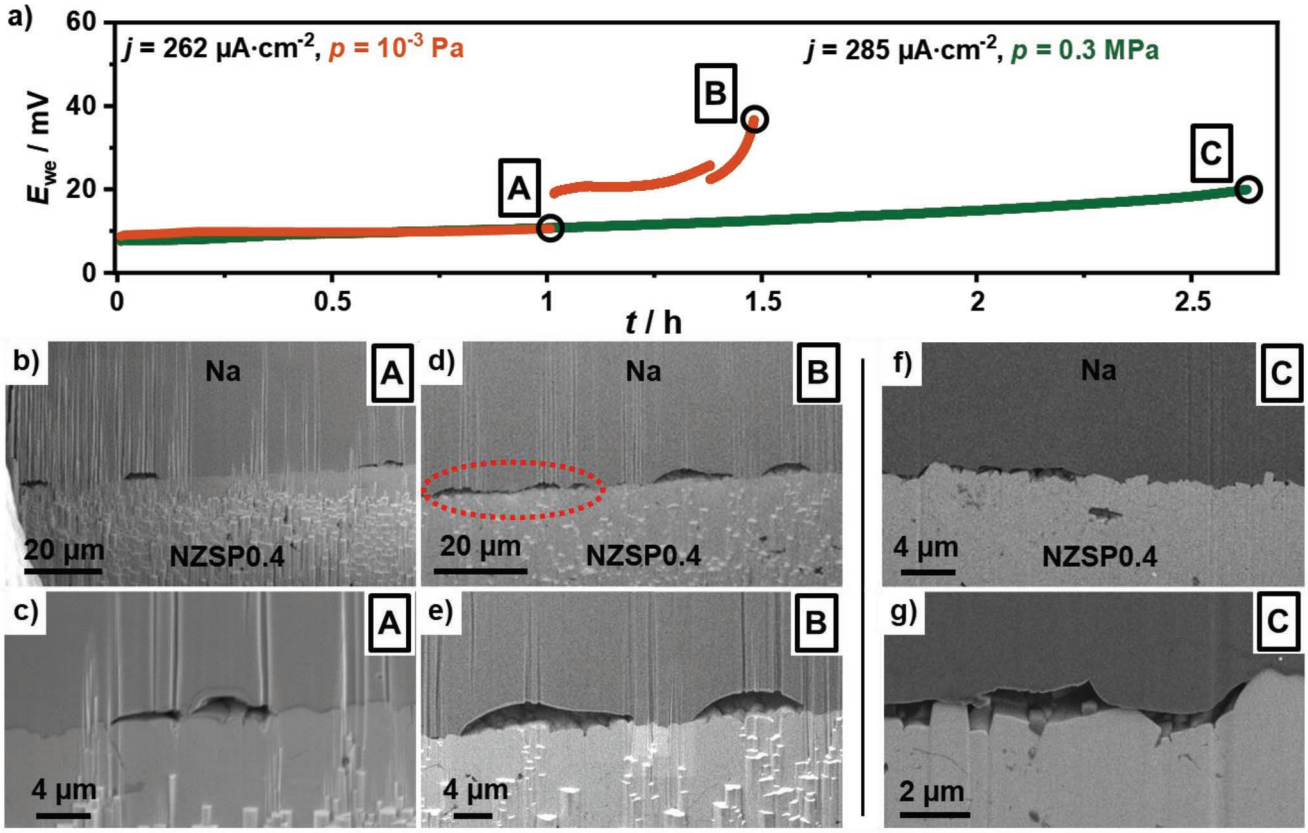

Figure 7. a) Voltage profile of a symmetric $Na_{id}|NZSP0.4|Na_{id}$ cell in which one electrode was anodically dissolved in vacuum (orange) and at an external pressure of 0.3 MPa (green). The marked points A, B, and C show after which dissolution times cross-sections of the interface have been prepared and investigated. Cross-section of the Na|NZSP0.4 interface after a dissolution time of 1 h in vacuum at b) low and c) high magnification. Cross-section of the interface after a dissolution time of 1.5 h in vacuum at d) low and e) high magnification. The red circle indicates an insulating gap at the interface. Cross-section after a dissolution time of 2.5 h with external load of 0.3 MPa at f) low and g) high magnification.

the cut-off voltage of 60 mV after 700 min a total amount of 28 µmol sodium was dissolved, which corresponds to a thickness of about 16 µm normalized to the geometric electrode area.

Following the anodic dissolution steps, the activation energies of the different resistance contribution were determined. The activation energies for bulk, grain boundary, and interface (see Table S4, Supporting Information) agree with the results of the previous section and give a consistent picture. Regardless of whether contact loss results from insufficient pressure during preparation or from anodic dissolution, the rate-limiting step is not affected. It is current constriction, which originates from the pores at the interface, thereby increasing the overvoltage.

The interface morphology formed during anodic dissolution was visualized by FIB-SEM cross-section. For preparation of the cross-section, the dissolution was paused and cells were transferred to the FIB-SEM system. After imaging the dissolution experiment with the same cell was continued. A strong dependence of the pore morphology on the applied external load is observed. Two symmetrical $Na_{id}|NZSP0.4|Na_{id}$ cells were assembled and anodic dissolution was carried out at different external loads. To minimize the influence of creep and plastic deformation driven by an external load on the formed pore morphology, dissolution of one cell was performed inside the vacuum of an SEM at a pressure of $p = 10^{-3}$ Pa. Detailed information on the experimental set up is given in the Experimental Section. The obtained potential profile is given in **Figure 7**a. Starting with a potential of about 8 mV, a constant voltage plateau at $E_{WE} = 10$ mV was observed within the first hour. In the subsequently recorded cross-sections at the interface in Figure 7b,c, individual and separate lens-shaped pores can be seen. However, a larger part of the sodium electrode is still in contact with the SE. Upon further dissolution, a potential step from 10 to 20 mV is observed, which is due to different temperatures during individual dissolution steps. Since the experiments were conducted inside an SEM, exact temperature control was not possible. After a total dissolution time of 80 min, the initially flat potential profile develops into a steep increase. To visualize the pore morphology before complete contact loss is approached, the dissolution was stopped at a cut-of voltage of 36 mV. An increase in pore size after the second dissolution step is obvious, while maintaining a lens-shaped form (Figure 7d,e). Besides the growth of pores, very shallow pores are also observed leading to a large insulating gap at the interface (Figure 6d red circle). Therefore, the interfacial contact area between sodium and NZSP0.4 is drastically reduced to a few contact points explaining the steep increase in overpotential.

In the second case, an external load of 0.3 MPa was applied, while a current density comparable to the previous cell was

used for anodic dissolution. At a comparable initial potential of 9 mV, no constant plateau was observed with an external pressure, but rather a linear increase until a cut-off voltage of 20 mV was reached (Figure 7a, green curve). Even after a dissolution time of 2.5 h, no steep increase of the potential was observed. The amount of sodium dissolved under low-potential conditions can be significantly increased with external pressure.

Compared to the previous cross-sections, no lens-shaped pores were obtained when dissolving anodically with external pressure. Still, large regions with interfacial contact are present at the interface (Figure 7f), while small pores were found only at some spots (Figure 7g). In these regions of contact loss, only "pillars" of the SE were still in contact with the electrode, while "valleys" were no longer in contact. Especially, small grains located in "valleys" were not contacted to the sodium electrode, introducing and enhancing the CC at this interface.

When comparing the result of the experiments conducted at different pressures, it must be noted that the time delay between the preparation of cross-sections and the end of anodic dissolution differed significantly. While a cross-section was prepared immediately after anodic dissolution in the SEM (at $p = 10^{-3}$ Pa), the external pressure of 0.3 MPa acted significantly longer in the corresponding experiment (10 h after end of anodic dissolution). A direct comparison between the two series of measurements is therefore challenging. Nevertheless, with an external pressure and a subsequent resting phase, a significantly higher amount of sodium can be dissolved without deteriorating the interfacial contact significantly.

2.4. Temporal Evolution of the Interface after Anodic Dissolution

Finally, the temporal evolution of the Na|NZSP0.4 interface after anodic dissolution was examined by impedance spectroscopy. For this purpose, a sodium anode in a symmetrical Na_{id}|NZSP0.4|Na_{id} cell was dissolved at a current density of 350 µA cm^{-2} under atmospheric pressure. Immediately after completion of the anodic dissolution, impedance spectra were recorded in intervals of 5 min to monitor the development of the interface behavior. To record changes of the interface during dissolution, galvanostatic electrochemical impedance spectroscopy (GEIS) was used.

Similar potential curves (**Figure 8**a) and a comparable impedance evolution (Figure 8b,c) were observed for continuous anodic dissolution, analogous to the successive dissolution in Figure 5a,c. After the dissolution had been finished, a strong decrease of the total resistance by several hundred Ω cm^2 is seen in Figure 8d,e. Within the first 20 min of this relaxation period the drop of resistance is pronounced. After 13 h of rest, the total resistance is only 7 Ω cm^2 higher than in the initial state indicating recovery of the interface. During the transition of the dissolution to the relaxation phase, a "swerving" as well as a "rolling in" of the impedance shape in the low-frequency range is monitored. The reason for this is the nonstationary interface state since significant changes of the interface take place during the impedance recording. This shows that strong relaxation effects occur at the interface directly after dissolution.

Following the resting phase, a second anodic dissolution of the same electrode was performed, whereby a potential curve similar to the first dissolution was obtained. In Figure 8f,g, the Nyquist plot of the pristine cells, after the dissolution and completion of the relaxation are shown. A decrease of impedance is also observed after a second dissolution step, which reached nearly the initial state indicating repeated equilibration at the Na|NZSP0.4 interface after continuous dissolution. Comparing the dissolved amounts of sodium, only one sixth (1.2 µm) could be dissolved during the second dissolution compared to the first dissolution step (7 µm). Thus, despite nearly identical impedances after resting, irreversible changes to the pristine interface are caused.

To check whether the observed and described equilibration is caused by the external load even when only atmospheric pressure was applied, the experiment was repeated at a pressure of 10^{-3} Pa. Figure S12 (Supporting Information) shows the potential curves and the impedances recorded during relaxation. Abrupt changes of the potential curve toward the end of the dissolution are probably due to the electronic contacting of the cell inside the vacuum chamber. The results obtained during the first dissolution step are identical to those obtained with atmospheric pressure. In the subsequent resting phase, also a decrease in total resistance is monitored, which indicates dynamic processes at the Na|NZSP0.4 interface even at extremely low external loads. Compared to the previous experiment, the equilibration of the interface after anodic dissolution is clearly less pronounced as the total resistance tends to a higher value (120 Ω cm^2) compared to the initial resistance of the pristine cell (42 Ω cm^2). Furthermore, only 73 nm of sodium can be dissolved in a following dissolution step.

We like to note that the quantity used to assess the equilibration of the interface is the current constriction contribution in the measured impedance. The impedance contribution of current constriction is affected by the properties characterizing an interface, e.g., contact area, pore size, and distribution of contact points.[34,35] Thus, the observed equilibration and the measured impedance contribution result from a change of the interfacial properties after dissolution and cannot be assigned only to an improvement of the contact area. Reduction of the pore size can occur through diffusion of vacancies into the bulk of the metal. Also, ad-atom diffusion can change the pore structure so that the surface energy is minimized (Ostwald ripening). Both processes show a pronounced time dependence with respect to changes in the pore morphology at the interface. Besides diffusion and energy minimization, mechanical properties of the metal electrode, especially creep, affect the interfacial pore morphology, too. Depending on temperature, microstructure (grain size and shape), dislocation density and applied stress, different mechanisms of creep dominate the deformation of polycrystalline materials. Due to the high homologous temperature and the low yield strength (0.2–0.3 MPa), deformation of sodium at room temperature and atmospheric pressure is mainly dominated by dislocation climbing, rate-limited by lattice diffusion.[46,47] At low external stress, the deformation of sodium is dominated by lattice diffusion, known as Nabarro–Herring creep.[70] Compared to diffusion-based creep mechanisms such as Nabarro–Herring and Coble creep, higher strain rates are obtained with dislocation creep, which explains the larger amount of dissolved sodium at higher external load.[44]

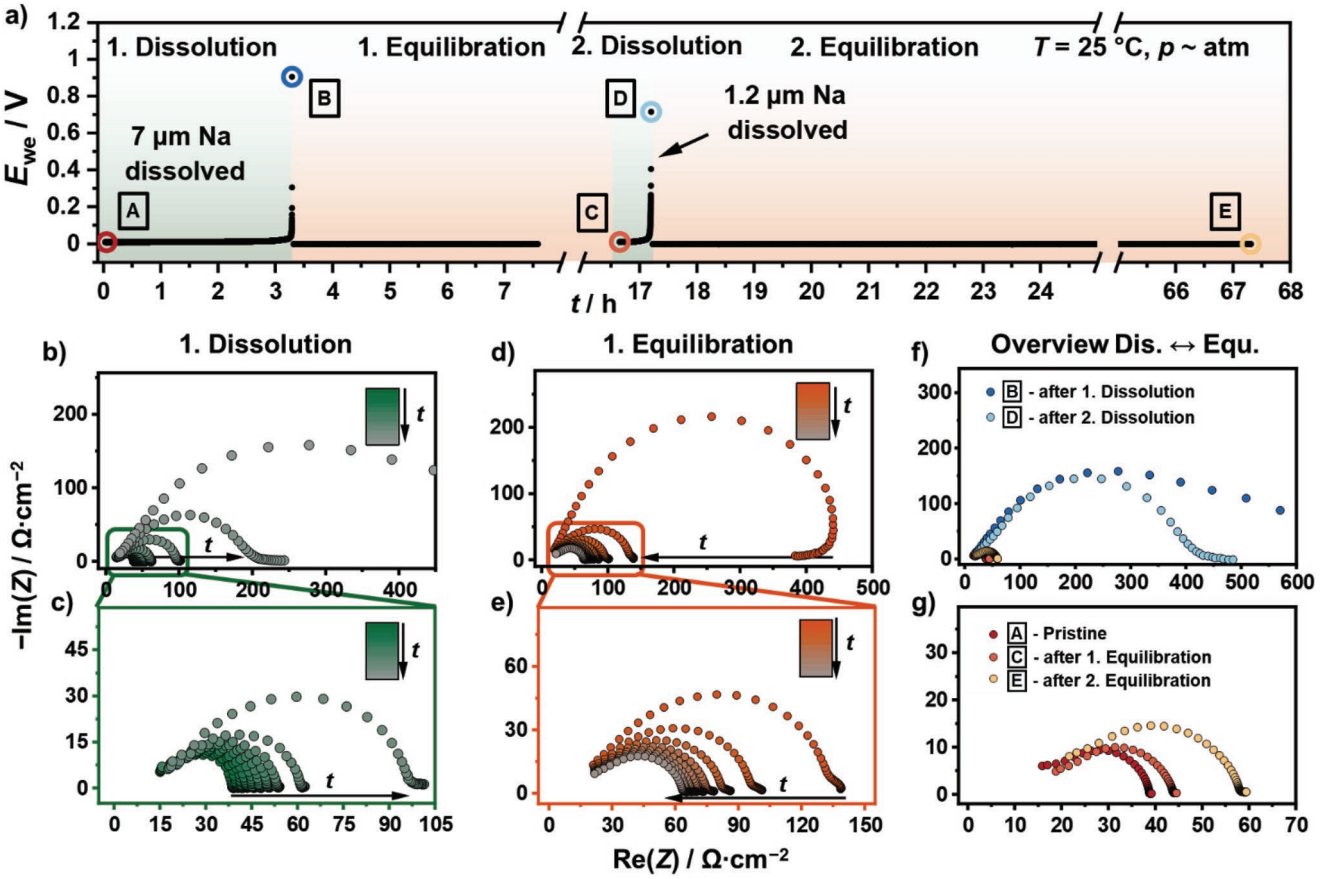

Figure 8. a) Voltage curve of a symmetric $Na_{id}|NZSP0.4|Na_{id}$ cell dissolved anodically by galvanostatic electrochemical impedance spectroscopy at a current density of 350 µA cm^{-2}. After reaching the cut-off voltage of 1 V, the electrode was analyzed by PEIS in intervals of 5 min until the change of the real part of the impedance is <1 Ω. The described procedure was repeated with the same electrode. b) Development of impedance (GEIS measurement) during anodic dissolution of the WE with an enlarged section in (c). Analogous to the previous measurements, impedance increases with increasing dissolution time. d) Obtained impedance data during equilibration period are shown in (d) and (e). A clear drop of the total resistance can be seen in (d), which is close to the original impedance. Representation of selected impedance spectra (marked as colored points in (a)) before and after a dissolution step as well as after completion of the relaxation of the entire measurement protocol are given in (f) and (g).

We assume that the observed interface equilibration is mainly due to creep of sodium, in addition to the minimization of surface energies and the annihilation of vacancies. When lowering the external stress to a minimum (10^{-3} Pa) equilibration is still observed, which is attributed to vacancy diffusion, meaning diffusion due to a concentration gradient. Since creep is pressure- and time-dependent, the amount of sodium that can be dissolved after equilibration is also determined by the dissolution protocol. For instance, a stepwise dissolution could dissolve significantly more sodium (16 µm) compared to a continuous dissolution (7 µm), similarly to the effect of a discontinuous charging and discharging protocols known from rechargeable lithium metal[71] or lithium-ion-batteries.[72] This is especially crucial for real battery applications, in which significantly different dissolution protocols would be needed depending on the required application.

3. Conclusions

In this study, a detailed electrochemical analysis of the interfacial behavior of NZSP0.4 in contact with sodium is presented. Exploring its thermodynamic stability, the formation of a kinetically stabilized interlayer (SEI) within 4 h after contacting through the reduction of zirconium monitored by in situ XPS was observed. The influence of the formed interphase resistance $R_{Interphase}$ is below 2 Ω cm^2 and could not be fully resolved by impedance spectroscopy, but clearly identified by TEM. We conclude that the SEI formation of NZSP0.4 allows stable operation of the sodium anode.

In the next step, we measured the interfacial impedance at different pressures and temperatures under equilibrium conditions. We found that the interface contribution to the impedance spectrum at low frequencies is caused by current constriction, i.e., by non-ideal physical contact between sodium and NZSP0.4 due to insufficient mechanical pressure. Based on the similarity of the determined activation energies for $E_{a,Int}$ and $E_{a,GB}$, as well as a completely vanishing interfacial resistance at high mechanical pressures, neither the formed SEI nor the charge transfer limit the ion transport across the Na|NZSP0.4 interface.

Third, we studied the formed interfacial morphology at the Na|NZSP0.4 interface during anodic dissolution of the metal

electrode at different external loads. Impedances recorded during anodic dissolution support the conclusion of current constriction being the origin of the interfacial resistance R_{Int}. Visualization of the interfacial morphology by FIB-SEM after anodic dissolution reveals the formation of lens-shaped pores when no external pressure was applied during dissolution, whereas with external load, smaller, shallower insulating gaps were observed.

Finally, the temporal evolution of the interfacial morphology after anodic dissolution was analyzed by means of time-resolved impedance spectroscopy. Independent of an external pressure, a decrease of the interfacial contribution with time was observed in the impedance spectra after anodic dissolution, which we interpret as dynamic change of the interfacial pore structure. The cause of equilibration without external pressure is attributed to diffusion of vacancies (like Nabarro–Herring creep) as well as ad-atoms. Applying an external pressure leads to a pronounced equilibration which is attributed to a more enhanced dislocation creep of sodium. Accordingly, for real battery applications, resting periods for equilibration of interfaces play a central role to maintain interfacial contact in addition to external load.

To gain a better understanding of the equilibration, further studies are necessary regarding the influence of current density and temperature. Based on the results, the sodium metal anode could show less degradation due to pore formation during cell discharge compared to the lithium metal anode especially in low temperature regions—which may also reduce the dendrite risk during charging.

4. Experimental Section

Synthesis of Solid Electrolyte: NZSP0.4 powder was synthesized on a 1 kg scale using a solution-assisted solid-state reaction method (SA-SSR).[16] $NaNO_3$ (VWR), $ZrO(NO_3)_2$ (Aldrich), $Si(OCH_2CH_3)_4$ (Merck), and $NH_4H_2PO_4$ (Merck) were used as starting materials with a purity of >99%. Stoichiometric amounts of $NaNO_3$ and $ZrO(NO_3)_2$ were dissolved in deionized water. A stoichiometric amount of $Si(OCH_2CH_3)_4$ was also added to the solution while stirring. When $Si(OCH_2CH_3)_4$ was hydrolyzed, the stoichiometric amount of $NH_4H_2PO_4$ was added to the system during stirring. The whole mixture was dried at 85 °C. The dried powder was calcined at 800 °C for 3 h. After calcination, a white powder was obtained. The calcined powder was then milled in ethanol with zirconia balls on a milling bench for 48 h, and dried at 70 °C for 12 h. NZSP0.4 powder was put into a cylindrical pressing mold (diameter of 13 mm) and pressed with a uniaxial pressure of about 100 MPa at room temperature. The pressed pellets were sintered at 1280 °C for 5 h. The obtained pellets were white in color and had a thickness of about 2 mm and a diameter of 10 mm. The relative density of the sintered pellets was >95%.

Materials Characterization: The synthesized NZSP0.4 SE was characterized using a PANalytical Empyrean powder diffractometer in Bragg–Brentano Θ–Θ geometry. A Cu K$\alpha_{1,2}$ radiation ($\lambda(\alpha_1) = 1.540\,596$ Å, $\lambda(\alpha_2) = 1.544\,410$ Å) X-ray source was used and operated at 40 kV and 40 mA. Measurements were recorded in the 2Θ range of 10°–90° with a step size of 0.026° using a PIXcel3D 1×1 detector. For the measurement, the sample was manually ground and placed on a (911) orienting silicon zero background holder. Examinations of the microstructure of the surface were carried out using a Carl Zeiss Ultra field emission SEM instrument (Merlin). Surface roughness of the SE was determined using a profilometer (Alpha-Step D-600 Stylus, KLA Tencor). The R_a value was averaged from three measurements with a scan length of 0.5 mm and a force of 1 mg.

Cell Assembling/Preparation: For electrochemical characterization of bulk and grain boundary properties, symmetrical Au|NZSP0.4|Au cells with blocking electrodes were analyzed. Gold electrodes with thicknesses of 200 nm were prepared by thermal evaporation. The electrode area was determined by evaluating optical images of the electrodes utilizing the software package ImageJ.[73] NZSP0.4 was used without any further surface treatment or polishing step. Afterward the cells were sealed in pouch bags to ensure inert atmosphere during measurements.

All impedance measurements for the study of the interfaces were performed on symmetrical Na|NZSP0.4|Na cells. A straightforward analysis of both interfaces by impedance spectroscopy is only possible in the case of identical interfaces in equilibrium. If this condition is not fulfilled, the introduction of a reference electrode is necessary to distinguish both interfaces. Since establishing a reference electrode for ceramic solid electrolytes is challenging, a QRE was used to monitor changes in an interface as has been shown for the Li|LLZO interface.[33] Using a two-electrode setup, one electrode has to be a resistance-free quasireversible interface, as demonstrated by Krauskopf et al.[33] By applying high external pressure, a virtually resistance-free interface Na|NZSP0.4 has also been obtained (see results). If a "normal" sodium electrode (working electrode, WE) with a higher interfacial resistance is combined with a QRE Na|NZSP0.4 half-cell, the contribution of the CE is minimized, and quasi only the WE is monitored.

For preparation of QRE Na|NZSP0.4 half-cells sodium foils were freshly prepared in an Ar-filled glovebox. Surface impurities were mechanically removed from a sodium ingot. The resulting clean sodium was pressed gradually to a foil with a thickness of ≈150 µm using a hand press. Electrodes with a diameter of 6 mm were then punched out and attached to a copper foil (10 mm in size). Before placing the sodium foil on the SE, the sodium surface was mechanically cleaned again. The other side of the SE was covered with a thin copper foil to protect the surface during the pressing process. Subsequently, the sodium foil was pressed onto the SE with a uniaxial load of 11 MPa for 1 min. For pressure control, an in-house built pressure setup equipped with a compression load cell FC22 (TE Connectivity) was used. Afterward, the cells were vacuum-sealed four times in plastic envelopes (CPR GmbH, Sonodome) and pressed isostatic at 100 MPa for 15 min at room temperature. To ensure that the formation of the interlayer was complete, the QRE half-cells were stored for 24 h in Ar atmosphere. The preparation of the sodium WEs varied and will be described for each experiment individually. A schematic illustration of the preparation process is shown in Figures S13 (Supporting Information).

To study the influence of pressure on the Na|NZSP0.4 interface, a sodium foil was pressed onto a QRE half-cell. Thereto, the cell was sandwiched between two Ni current collectors in a home-made pressure setup. The targeted pressure was maintained for 20 s and released afterward to a base load corresponding to 1 N (about 20 kPa). Reaching the base pressure, impedance spectra were recorded in the frequency range between 7 MHz and 10 Hz with a voltage amplitude of 10 mV using an SP-300 potentiostat (BioLogic Sciences Instruments). Afterward, the force was increased to a higher value than before, maintained for 20 s and released to the base pressure, followed by an impedance measurement. The procedure was repeated several times until a force of 215 N (about 4.2 MPa) was reached. The experiment was conducted in an Ar-filled glove box at room temperature.

For time-dependent impedance measurements, sodium WE was attached on a NZSP0.4|Na_{id} QRE half-cell using a uniaxial pressure of 11 MPa for 1 min. Directly after assembly, impedances were measured at intervals of 5 min with the previously described SP-300 potentiostat in the frequency range between 7 MHz and 100 Hz. To account for temperature fluctuations inside the glovebox, a thermocouple 306 (VOLTCRAFT) was placed next to the cell, tracking the temperature every minute.

Temperature dependence of symmetrical Na|NZSP0.4|Na and Au|NZSP0.4|Au cells was studied inside a climate chamber LabEvent

(Weisstechnik) between –40 and 40 °C. Impedance spectra were recorded in the frequency range from 7 MHz to 1 Hz with a voltage amplitude of 10 mV using a VMP-300 (BioLogic Sciences Instruments) potentiostat. Cells were sealed in pouch bags to ensure inert atmosphere during measurement.

GEIS measurements were performed in the frequency range between 7 MHz and 100 Hz with an applied direct current of about 300 µA cm^{-2} and a current amplitude of 30 µA cm^{-2} using SP-150 or VMP-300 potentiostats (BioLogic Sciences Instruments). Experiments under vacuum conditions were carried out inside an SEM chamber. The cells were contacted via a micromanipulator. A detailed explanation of the set-up and methodology is given in literature.[74,75] After the anodic dissolution was completed, PEIS measurements were performed in intervals of 7 min to monitor relaxation of the interface using the same instrumental parameters as described above.

Impedance data were analyzed by using Relaxis3 software (rhd instruments). Data points in the higher and lower frequency range with a relative error greater than 5% in Kramers–Kronig tests were not included in the data evaluation. Impedance spectra recorded above –30 °C were fitted with an additional *RQ*-element as the SE bulk contribution shifts into the measured frequency range. In impedance spectra below –30 °C the bulk contribution is described by a simple resistor. To eliminate the temperature variation of the time-dependent measurement series in the glovebox, the real part of the impedance was corrected as described in the Supporting Information. All impedance spectra were normalized to the geometric electrode area unless otherwise stated. The thickness of the SE has to be considered additionally when bulk and grain boundary (GB) properties are examined, which is roughly 2 mm for the samples investigated.

DRT analyses were carried out with the software package Relaxis3 (rhd instruments). The real and imaginary parts were considered for the analysis and 200 points were used for interpolation. The second derivative of the distribution function $\gamma(\tau)$ was used in the Tikhonov regularization problem. Calculations were performed using a regularization parameter $\lambda = 10^{-6}$.

In Situ X-Ray Photoelectron Spectroscopy: All XPS analyses were performed with a PHI5000 Versa Probe II system (Physical Electronics GmbH). A home-built sample holder was used for sputtering sodium metal on top of the electrolyte. Detailed information about the sample holder and the procedure of the in situ XPS sputtering can be found in previous reports.[76] In short, sodium is attached to a sail with an 85° angle of inclination by using copper tape and aligned to an Ar^+-ion gun. The SE is attached underneath the sail with nonconductive adhesive tape. By sputtering the sodium foil, a plasma is generated through which sodium is deposited on the SE. The reaction layer (i.e., the interphase) obtained is subsequently characterized by XPS. Spectra were monitored as a function of deposition time on top of the electrolyte. Sputtering of sodium was carried out with 4 kV Ar^+-ion gun in intervals of 3 min with a total sputtering time of 60 min.

For analysis, monochromatic Al K_α radiation (1486.6 eV) was used. The X-ray source was operated at 50 W with a voltage of 17 kV and a beam diameter of 200 μm. Spectra were recorded with a step size and dwell time per step of 0.1 eV and 50 ms, respectively. A pass energy for the analyzer of 46.95 eV was used to record XP spectra between the sodium deposition steps. Additionally, for XP spectra before, directly after and 8 h after the sodium deposition were recorded with an analyzer pass energy of 23.5 eV. For charge neutralization a combination of ion and low-energy electron beam was applied during the measurements.

Data evaluation was carried out with the software CasaXPS (Version 2.3.22, Casa Software Ltd.). XP spectra were calibrated to 284.8 eV using the aliphatic carbon C 1s signal. A Shirley-type background with a Gaussian–Lorentzian function (GL(30)) line shape was utilized for the signal evaluation. Additionally, fitting constraints were used, such as the FWHM constraint, energy splitting values known in the literature due to spin–orbit coupling and the resulting area ratios.

Focused Ion Beam Scanning Electron Microscopy: Cross-sections of the electrode|SE interface were carried out with a XEIA3 system (TESCAN GmbH). Samples were attached to a Leica stub with adhesive copper tape and transferred using the Leica EM VCT500 system (Leica Microsystems GmbH). Before milling, the samples were cooled to –133 °C by liquid nitrogen and cooling was maintained during the analysis. Xe^+ ions with an energy of 30 kV were used in all experiments. Beam currents for milling and polishing were set to 2 µA and 30 nA. For preparation of the electron transparent specimen an Auriga system (Carl Zeiss NTS GmbH) with a liquid nitrogen stage (GATAN GmbH; operation temperature: –185 °C) has been used. Thinning process of the TEM lamella was performed using Ga^+ ions with 30 kV high tension energy and beam current of 240 pA.

Transmission Electron Microscopy: TEM analysis was performed at the aberration corrected (STEM) Themis 300 system (Thermo Fischer Scientific) using a beam energy of 300 kV and a screen current of 100 pA. EDX analysis was conducted with a Super-X EDX detector. Characterization was carried out under cryogenic conditions (–185 °C) using a liquid nitrogen cooled 915 cryo transfer holder (GATAN GmbH). Data evaluation was conducted using Velox software package (Thermo Fischer Scientific).

Supporting Information

Supporting Information is available from the Wiley Online Library or from the author.

Acknowledgements

This work contributes to the research performed at CELEST (Center for Electrochemical Energy Storage Ulm-Karlsruhe) and was funded by the German Research Foundation (DFG) under Project ID 390874152 (POLiS Cluster of Excellence). Financial support by the BMBF Cluster of Competence FESTBATT (S.B., Project No. 03XP0180) is also acknowledged. J.K.E. acknowledges financial support by the DFG via the GRK (Research Training Group) 2204 "Substitute Materials for sustainable Energy Technologies." The authors acknowledge the Karlsruhe Nano Micro Facility (KNMFi) at KIT for providing TEM access. Experimental support by Dr. Klaus Peppler and Dr. Boris Mogwitz (JLU Giessen) is acknowledged.

Open access funding enabled and organized by Projekt DEAL.

Conflict of Interest

The authors declare no conflict of interest.

Author Contributions

T.O., T.F., and S.B. designed the experiments. Q.M. prepared the solid electrolyte. T.O. performed all XPS experiments, impedance analysis and cross sections experiments. T.F. supported in situ SEM studies. T.O. and J.S. interpreted the XPS. T.O., S.B., J.K.E., and T.F. interpreted impedance analysis. Z.D. performed TEM sample preparation and characterization. T.O., Z.D., and C.K. interpreted TEM analysis. T.O., S.B., M.R., Q.M., and J.J. wrote the manuscript. All authors discussed the results and contributed to the preparation of the manuscript. C.K., O.G., and C.H. reviewed and edited the manuscript.

Data Availability Statement

The data that support the findings of this study are available from the corresponding author upon reasonable request.

Keywords

current constriction, impedance spectroscopy, interphase growth, NASICON electrolytes, SEI formation, sodium metal anodes

Received: August 8, 2022
Revised: September 28, 2022
Published online: December 23, 2022

[1] J. Janek, W. G. Zeier, *Nat. Energy* **2016**, *1*, 1167.
[2] B. Xiao, T. Rojo, X. Li, *ChemSusChem* **2019**, *12*, 133.
[3] J. Cui, A. Wang, G. Li, D. Wang, D. Shu, A. Dong, G. Zhu, J. Luo, B. Sun, *J. Mater. Chem. A* **2020**, *8*, 15399.
[4] X. Xia, C.-F. Du, S. Zhong, Y. Jiang, H. Yu, W. Sun, H. Pan, X. Rui, Y. Yu, *Adv. Funct. Mater.* **2022**, *32*, 2110280.
[5] M. D. Slater, D. Kim, E. Lee, C. S. Johnson, *Adv. Funct. Mater.* **2013**, *23*, 947.
[6] C. Monroe, J. Newman, *J. Electrochem. Soc.* **2004**, *151*, A880.
[7] Z. Zhang, Y. Shao, B. Lotsch, Y.-S. Hu, H. Li, J. Janek, L. F. Nazar, C.-W. Nan, J. Maier, M. Armand, L. Chen, *Energy Environ. Sci.* **2018**, *11*, 1945.
[8] U. von Alpen, M. Bell, H. Hofer, *Solid State Ionics* **1981**, *3–4*, 215.
[9] J. B. Goodenough, H. Y.-P. Hong, J. A. Kafalas, *Mater. Res. Bull.* **1976**, *11*, 203.
[10] Y. B. Rao, K. K. Bharathi, L. N. Patro, *Solid State Ionics* **2021**, *366–367*, 115671.
[11] Z. Yang, B. Tang, Z. Xie, Z. Zhou, *ChemElectroChem* **2021**, *8*, 1035.
[12] A. G. Jolley, G. Cohn, G. T. Hitz, E. D. Wachsman, *Ionics* **2015**, *21*, 3031.
[13] Q. Ma, M. Guin, S. Naqash, C.-L. Tsai, F. Tietz, O. Guillon, *Chem. Mater.* **2016**, *28*, 4821.
[14] Z. Zhang, Z. Zou, K. Kaup, R. Xiao, S. Shi, M. Avdeev, Y.-S. Hu, D. Wang, B. He, H. Li, X. Huang, L. F. Nazar, L. Chen, *Adv. Energy Mater.* **2019**, *9*, 1902373.
[15] J. A. Kafalas, J. R. Cava, in *Proc. Int. Conference on Fast Ion Transport in Solids, Electrodes, and Electrolytes* (Eds: P. Vashishta, J. N. Mundy, G. K. Shenoy), Elsevier North Holland, Amsterdam **1979**, pp. 419–422.
[16] Q. Ma, C.-L. Tsai, X.-K. Wei, M. Heggen, F. Tietz, J. T. S. Irvine, *J. Mater. Chem. A* **2019**, *7*, 7766.
[17] W. Zhou, Y. Li, S. Xin, J. B. Goodenough, *ACS Cent. Sci.* **2017**, *3*, 52.
[18] X. Yu, A. Manthiram, *Matter* **2019**, *1*, 439.
[19] J. Yang, Z. Gao, T. Ferber, H. Zhang, C. Guhl, L. Yang, Y. Li, Z. Deng, P. Liu, C. Cheng, R. Che, W. Jägermann, R. Hausbrand, Y. Huang, *J. Mater. Chem. A* **2020**, *8*, 7828.
[20] E. Matios, H. Wang, C. Wang, X. Hu, X. Lu, J. Luo, W. Li, *ACS Appl. Mater. Interfaces* **2019**, *11*, 5064.
[21] T. Wu, Z. Wen, C. Sun, X. Wu, S. Zhang, J. Yang, *J. Mater. Chem. A* **2018**, *6*, 12623.
[22] X. Miao, H. Di, X. Ge, D. Zhao, P. Wang, R. Wang, C. Wang, L. Yin, *Energy Storage Mater.* **2020**, *30*, 170.
[23] X. Chi, F. Hao, J. Zhang, X. Wu, Y. Zhang, S. Gheytani, Z. Wen, Y. Yao, *Nano Energy* **2019**, *62*, 718.
[24] M. M. Gross, L. J. Small, A. S. Peretti, S. J. Percival, M. A. Rodriguez, E. D. Spoerke, *J. Mater. Chem. A* **2020**, *8*, 17012.
[25] H. Fu, Q. Yin, Y. Huang, H. Sun, Y. Chen, R. Zhang, Q. Yu, L. Gu, J. Duan, W. Luo, *ACS Mater. Lett.* **2020**, *2*, 127.
[26] Y. Uchida, G. Hasegawa, K. Shima, M. Inada, N. Enomoto, H. Akamatsu, K. Hayashi, *ACS Appl. Energy Mater.* **2019**, *2*, 2913.
[27] J. A. S. Oh, Y. Wang, Q. Zeng, J. Sun, Q. Sun, M. Goh, B. Chua, K. Zeng, L. Lu, *J. Colloid Interface Sci.* **2021**, *601*, 418.
[28] M.-C. Bay, M. Wang, R. Grissa, M. V. F. Heinz, J. Sakamoto, C. Battaglia, *Adv. Energy Mater.* **2020**, *10*, 1902899.
[29] E. Quérel, I. D. Seymour, A. Cavallaro, Q. Ma, F. Tietz, A. Aguadero, *J. Phys. Energy* **2021**, *3*, 44007.
[30] C.-L. Tsai, T. Lan, C. Dellen, Y. Ling, Q. Ma, D. Fattakhova-Rohlfing, O. Guillon, F. Tietz, *J. Power Sources* **2020**, *476*, 228666.
[31] D. S. Jolly, Z. Ning, J. E. Darnbrough, J. Kasemchainan, G. O. Hartley, P. Adamson, D. E. J. Armstrong, J. Marrow, P. G. Bruce, *ACS Appl. Mater. Interfaces* **2020**, *12*, 678.
[32] H. Koshikawa, S. Matsuda, K. Kamiya, M. Miyayama, Y. Kubo, K. Uosaki, K. Hashimoto, S. Nakanishi, *J. Power Sources* **2018**, *376*, 147.
[33] T. Krauskopf, H. Hartmann, W. G. Zeier, J. Janek, *ACS Appl. Mater. Interfaces* **2019**, *11*, 14463.
[34] J. K. Eckhardt, P. J. Klar, J. Janek, C. Heiliger, *ACS Appl. Mater. Interfaces* **2022**, *14*, 35545.
[35] J. K. Eckhardt, T. Fuchs, S. Burkhardt, P. J. Klar, J. Janek, C. Heiliger, *ACS Appl. Mater. Interfaces* **2022**, *14*, 42757.
[36] J. Fleig, *Solid State Ionics* **1998**, *113–115*, 739.
[37] S.-K. Otto, T. Fuchs, Y. Moryson, C. Lerch, B. Mogwitz, J. Sann, J. Janek, A. Henss, *ACS Appl. Energy Mater.* **2021**, *4*, 12798.
[38] T. Krauskopf, F. H. Richter, W. G. Zeier, J. Janek, *Chem. Rev.* **2020**, *120*, 7745.
[39] C. Wang, H. Jin, Y. Zhao, *Small* **2021**, *17*, e2100974.
[40] S. Ohno, T. Bernges, J. Buchheim, M. Duchardt, A.-K. Hatz, M. A. Kraft, H. Kwak, A. L. Santhosha, Z. Liu, N. Minafra, F. Tsuji, A. Sakuda, R. Schelm, S. Xiong, Z. Zhang, P. Adelhelm, H. Chen, A. Hayashi, Y. S. Jung, B. V. Lotsch, B. Roling, N. M. Vargas-Barbosa, W. G. Zeier, *ACS Energy Lett.* **2020**, *5*, 910.
[41] J. Janek, *Solid State Ionics* **1997**, *101*, 721.
[42] S. Majoni, J. Janek, *Ber. Bunsengesellschaft phys. Chem.* **1998**, *102*, 756.
[43] M. Rohnke, C. Rosenkranz, J. Janek, *Solid State Ionics* **2006**, *177*, 447.
[44] P. M. Sargent, M. F. Ashby, *Scr. Metall.* **1984**, *18*, 145.
[45] A. Schröder, J. Fleig, D. Gryaznov, J. Maier, W. Sitte, *J. Phys. Chem. B* **2006**, *110*, 12274.
[46] M. J. Wang, J.-Y. Chang, J. B. Wolfenstine, J. Sakamoto, *Materialia* **2020**, *12*, 100792.
[47] C. D. Fincher, Y. Zhang, G. M. Pharr, M. Pharr, *ACS Appl. Energy Mater.* **2020**, *3*, 1759.
[48] D. K. Singh, T. Fuchs, C. Krempaszky, P. Schweitzer, C. Lerch, F. H. Richter, J. Janek, *Adv. Funct. Mater.*, https://doi.org/10.1002/adfm.202211067.
[49] H. Tang, Z. Deng, Z. Lin, Z. Wang, I.-H. Chu, C. Chen, Z. Zhu, C. Zheng, S. P. Ong, *Chem. Mater.* **2018**, *30*, 163.
[50] V. Lacivita, Y. Wang, S.-H. Bo, G. Ceder, *J. Mater. Chem. A* **2019**, *7*, 8144.
[51] J. Maier, U. Warhus, E. Gmelin, *Solid State Ionics* **1986**, *18–19*, 969.
[52] Z. Zhang, S. Wenzel, Y. Zhu, J. Sann, L. Shen, J. Yang, X. Yao, Y.-S. Hu, C. Wolverton, H. Li, L. Chen, J. Janek, *ACS Appl. Energy Mater.* **2020**, *3*, 7427.
[53] S. Wang, H. Xu, W. Li, A. Dolocan, A. Manthiram, *J. Am. Chem. Soc.* **2018**, *140*, 250.
[54] Z. Gao, J. Yang, H. Yuan, H. Fu, Y. Li, Y. Li, T. Ferber, C. Guhl, H. Sun, W. Jägermann, R. Hausbrand, Y. Huang, *Chem. Mater.* **2020**, *32*, 3970.
[55] Z. Bastl, A. I. Senkevich, I. Spirovová, V. Vrtílková, *Surf. Interface Anal.* **2002**, *34*, 477.
[56] C. Morant, J. M. Sanz, L. Galán, L. Soriano, F. Rueda, *Surf. Sci.* **1989**, *218*, 331.
[57] S. P. Kowalczyk, L. Ley, F. R. McFeely, R. A. Pollak, D. A. Shirley, *Phys. Rev. B* **1973**, *8*, 3583.
[58] Q. Wu, *Solid State Ionics* **2004**, *167*, 155.
[59] A. Barrie, F. J. Street, *J. Electron Spectrosc. Relat. Phenom.* **1975**, *7*, 1.
[60] Z. Gao, J. Yang, G. Li, T. Ferber, J. Feng, Y. Li, H. Fu, W. Jägermann, C. W. Monroe, Y. Huang, *Adv. Energy Mater.* **2022**, *12*, 2103607.

[61] K. Song, D. A. Agyeman, M. Park, J. Yang, Y.-M. Kang, *Adv. Mater.* **2017**, *29*, 1606572.
[62] B. Lee, D.-H. Seo, H.-D. Lim, I. Park, K.-Y. Park, J. Kim, K. Kang, *Chem. Mater.* **2014**, *26*, 1048.
[63] B. Verlinden, *Thermo-Mechanical Processing of Metallic Materials*, Elsevier, Amsterdam **2010**.
[64] X. Zhang, Q. J. Wang, K. L. Harrison, S. A. Roberts, S. J. Harris, *Cell Rep. Phys. Sci.* **2020**, *1*, 100012.
[65] J. T. S. Irvine, D. C. Sinclair, A. R. West, *Adv. Mater.* **1990**, *2*, 132.
[66] J. Fleig, J. Maier, *J. Electroceram.* **1997**, *1*, 73.
[67] J. Fleig, J. Maier, *Electrochim. Acta* **1996**, *41*, 1003.
[68] J. K. Eckhardt, S. Burkhardt, J. Zahnow, M. T. Elm, J. Janek, P. J. Klar, C. Heiliger, *J. Electrochem. Soc.* **2021**, *168*, 090516.
[69] J. Kasemchainan, S. Zekoll, D. S. Jolly, Z. Ning, G. O. Hartley, J. Marrow, P. G. Bruce, *Nat. Mater.* **2019**, *18*, 1105.
[70] J. Fiala, L. Kloc, J. Čadek, *Mater. Sci. Eng., A* **1991**, *137*, 163.
[71] M. Z. Mayers, J. W. Kaminski, T. F. Miller, *J. Phys. Chem. C* **2012**, *116*, 26214.
[72] S. Zhu, C. Hu, Y. Xu, Y. Jin, J. Shui, *J. Energy Chem.* **2020**, *46*, 208.
[73] C. A. Schneider, W. S. Rasband, K. W. Eliceiri, *Nat. Methods* **2012**, *9*, 671.
[74] T. Krauskopf, R. Dippel, H. Hartmann, K. Peppler, B. Mogwitz, F. H. Richter, W. G. Zeier, J. Janek, *Joule* **2019**, *3*, 2030.
[75] T. Krauskopf, B. Mogwitz, H. Hartmann, D. K. Singh, W. G. Zeier, J. Janek, *Adv. Energy Mater.* **2020**, *10*, 2000945.
[76] S. Wenzel, T. Leichtweiss, D. Krüger, J. Sann, J. Janek, *Solid State Ionics* **2015**, *278*, 98.